NTNU
Det skapende universitet

Carbon Dioxide Intercalation in Sodium Fluorohectorite Clay

Erlend Granbo Rolseth

Fysikk
Oppgaven levert: Mai 2011
Hovedveileder: Jon Otto Fossum, IFY

Norges teknisk-naturvitenskapelige universitet

Carbon Dioxide Intercalation in Sodium Fluorohectorite Clay

Erlend Granbo Rolseth

May 15, 2011

Abstract

Wide Angle X-ray Scattering (WAXS) measurements of the layered synthetic silicate sodium fluorohectorite (NaFh) when exposed to pressurized carbon dioxide are reported. With a custom made sample holder placed on top of a cooling system, measurements of the NaFh were taken at different conditions for temperature and pressure. The interlamellar spacing of the clay particles was observed to expand $\sim$2.4 Å in the 001-direction when the sample was held at -20°C and exposed to 15 bar of CO_2 for over 9 days, indicating the intercalation of CO_2. The d-spacing after intercalation is indistinguishable from the d-spacing of NaFh in the 1 Water Layer hydration state. The rate of intercalation process was demonstrated to be dependent on the temperature and the pressure of CO_2, with the decrease of temperature and the increase of pressure beeing favorable for intercalating CO_2. Through various experimental measurements the possibillity of water as the observed intercalated guest substance could be ruled out. Existing molecular models based on the swelling free energy are proposed to explain some of the features observed in the present experiment.

Contents

Preface

This thesis marks the closure of my Master degree in Physics at the Norwegian University of Technology and Science (NTNU). The work has been carried out at the Complex Systems and Soft Materials Group at NTNU and at the MAX-lab in Lund Sweden. During the last two years I have been so privileged to have learned about and attained 'hands-on' experience with tools such as Synchrotron X-ray and Complex' own SAXS/WAXS-machine. The experience has personally been very rewarding and a good motavating factor in the experimenntal work and in the writing of the thesis you are currently holding in your hands.

Motivation

The behavior of Na-fluorohectorite at different humidities has previously been studied [1, 2, 3, 4] and investigated with the use of Wide Angle X-ray Scattering (WAXS). The aim of this experiment has been to find out how CO_2 behaves together with Na-fluorohectorite, and especially if CO_2 intercalates in the interlamellar space in the same way as water vapor. This should be carried out with the use of the same technique (WAXS) as with the similar water vapor intercalation experiments. The basis of this work was to create reproducible experiments, where clay samples could be exposed to a controlled environment, where the temperature and pressure could be varied in the studies of clays interaction with CO_2. When knowing the phase diagram of carbon dioxide one can have a clear connection between the phase of the CO_2 and the behavior of the clay when exposed to it. A change in the basal d-spacing corresponding to the size of the CO_2 molecule would indicate that the CO_2 intercalates in the interlamellar space, in the same way as the water. Only a few experimental studies exist on the interaction of clays and CO_2 [5, 6].

Acknowledgments

I would like to start by thanking my supervisor, Jon Otto Fossum, for giving me the opportunity to work within such a fine research environment of inspiring people and excellent laboratory equipment. To be able to visit some of Europe's first-class synchrotron facilities and work with such a interesting topic has been both exciting and educational, and this have certainly been the most rewarding time of my studies so far. A huge thankyou also goes to Henrik Hemmen, whom I for a long time thought was, and therefore used as, my co-supervisor. Eventually it turned out he was not, but whenever I asked, he always offered a helping hand, useful advice or gave me helpful comments. His computer skills have been invaluable to my work. I would like to thank Ole Tore Buset for solving all the technical problems that I may or may not have caused, Tor Arne Vassdal for managing to build an excellent sample holder based of my awkward drawings and Elisabeth Lindbo Hansen and Davì de Miranda Fonsêca for their cooperation, company and sharing of chocolate during the long hours of the experiment at MAX-lab. A fatherly thanks goes to Sverre Rolseth for proofreading and giving comments on my work. Last, but not least, I also want to thank my family and friends for all the encouraging words and support.

Chapter 1

Theory

1.1 Clays

Clays are fascinating materials with applications that have played important roles throughout the human history [7]. Their ability to be easily shaped when wet, but become hard as rock when heated, is just one of the amazing properties that reveals a substance with interesting physical features. Clays can be found almost everywhere on earth. The abundance of them, together with the fact that they are inexpensive and environment friendly have led some to recognize them as the materials of the 21st century [8]. Although beeing studied and discussed by geologist, geo-chemists, geophysicists and others, for centuries, it is only during the last couple of decades they have been a subject for studies and applications beyond these traditional approaches and disciplines. The majorities of clays found in nature are typically not phase pure, and have therefore for a long time been undesirable for industrial use. The availability of clean chemistry-customized synthetic clays has however caused a growth of scientific interest and activity to the field, and new studies have shown that clays also have unique electrical, mechanical and rheological properties [9]. This has placed clays in the same group as other complex materials such as liquid crystals, colloids, polymers and bio materials [7].

1.1.1 Clay structure

Clays are divided into different subgroups depending on their structure, what kind of atoms they contain and their layer charge. The clay structure can be described by a composition of tetrahedral and octahedral sheets. One tetrahedron consists of a cation to four oxygen atoms (O) and a octahedron consist of a cation to six oxygen atoms or hydroxyls (OH^-)[1]. How these two types of sheets are joined together determines the structure of the clay. The 1:1 layer

[1] Common tetrahedron cations are Si^+, Al^{3+} and Fe^{3+}. Common octahedron cations are Al^{3+} and Mg^{2+}.

structure consists of the repition of one tetrahedral and one octahedral sheet. The 2:1 layer structure on the other hand, is the repetition of one octahedral sheet sandwiched between two tetrahedral sheets. In the 2:1 structure there is also a variation where *interlayer* or *guest* cations are positioned between the layers [8]. Figure 1.1 shows models of a 1:1 and 2:1 layer structure.

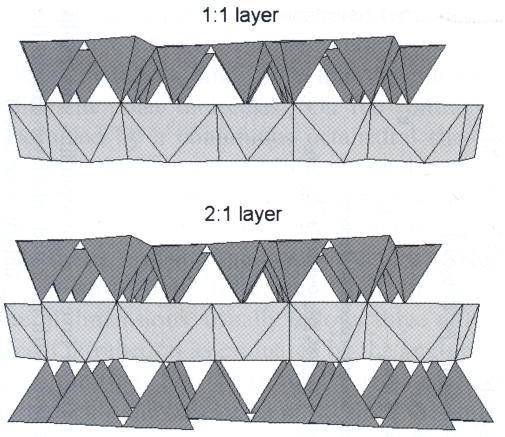

Figure 1.1: The figure shows the composition of tetrahedral (dark gray) and octahedral (light gray) sheets making up one layer in the 1:1 layer structure (top) and the 2:1 layer structure (bottom). Adapted from [8].

Clay particles are best described as disc-shaped, and can be made up of hundreds of 1:1 or 2:1 layers stacked on top of each other. A clay powder consist of thousands of such particles.

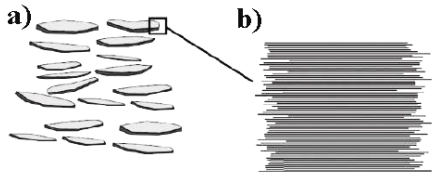

Figure 1.2: A clay particle (a) can be made out of hundreds of stacked layers (b).

Unit cell

Like other crystal structures, clays are categorized by their unit cell. For the 1:1 layer structure the unit cell consists of six octahedral sites and four tetrahedral sites, whereas six octahedral and eight tetrahedral sites makes up the unit cell for the 2:1 layer. For the 2:1 layer clays, the structures where all six octahedral

sites are occupied, are known as trioctahedral, while structures where only four octahedral sites are occupied are known as dioctahedral. The structural formula of the unit cell is often reported on the basis of the half unit cell [8]. The basal spacing, d_{001} (see figure 1.3), of the clay is defined as the distance from a certain plane in one layer to the closest corresponding plane in another parallel layer of the crystal. It thus also includes the features of the geometry of stacking of layers, as well as any material present between the layers [9].

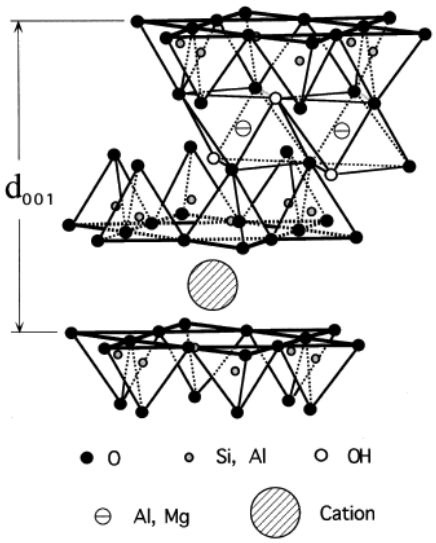

Figure 1.3: The structure of a 2:1 layer clay with a interlayer cation. The basal spacing d_{001} includes the features of the geometry of stacking of layers and possible guest substances between the layers. Adapted from [10].

Layer charge

A layer charge arises when the tetrahedral and octahedral sheets are joined together to form a layer [8]. It can then be either electrically neutral or negatively charged and is a sum of variable and permanent charges. The variable charges are due to the acid/base properties of the hydroxyl groups, and occurs at the edges of the clay layers. However, for most of the 2:1 layered clays the variable charges are significantly lower than the permanent charges, and can in those cases be neglected. The permanent negative layer charge arises from non-equivalent substitution of the central atoms whitin the octahedral or tetrahedral sheets. The charge on the crystalline layers induces a occupancy of exchangeable cations in the interlayer space (see figure 1.3), which balances the negative surface charge of the layers. The attractive electrostatic forces provides as short as possible distance between the negatively charged sites and the positively charged cations [11].

1.1.2 Swelling/Intercalation

The phenomenon of swelling/intercalation is one of the most remarkable characteristics of clays. The clays that possess this ability are termed smectite. Although other layered solids intercalate, the number of guest substances that can successfully be intercalated in clays grately exceeds those for the other classes of layered compounds. Intercalation occurs when guest substances are incorporated in the space between the layers causing the unit cell to expand, but without distorting the structure in any essential way. The space between the layers, originally occupied only by the interlayer cation, is often termed the *guest layer* or *interlayer space* because of this ability to incorporate substances. The joined tetrahedral and octahedral sheets on the other hand is termed the *host layer*. The intercalation process is dependent on the layer charge and the contributing Coulomb interaction between interlayer cations and the intercalated molecules [10].

The intercalation of water vapor, hydrating the interlayer cations, is the most common type of intercalation. The discrete number of water layers or hydration states resulting from this type of intercalation is often labeled 0WL, 1WL, 2WL and 3WL for the different layers respectively. The amount of water a clay is able to intercalate depends on the layer charge of that certain type of clay and on the water vapor pressure around the clay particles. A hydrated clay is a complex system, and the hydration dynamics and the detailed interactions between the interlayer cation, coordinating molecules and the charged clay surface are still not fully understood [2].

Whereas the intercalation of water has been a subject to many studies, fewer reports exist of CO_2 intercalation. More recently there have been carried out some experimental studies and computer simulations, that show the possibility of intercalation and retention of CO_2 in smectites. This have led the same people to believe that clay minerals can provide a distinctive material for carbon capture and carbon dioxide sequestration [12].

1.1.3 Hectorite

Hectorite is a trioctahedral smectite, which is composed of silicon tetrahedrons (SiO_4) and octahedrons of hydroxyls and magnesium (Mg-) and lithium (Li)-ions. Hectorites get their name from Hector, which is the area in California where they were first found. The composition of hectorite is expressed as

$$[M_x \times \mathrm{nH_2O}][(\mathrm{Mg}_{3-x}\mathrm{Li}_x)\mathrm{Si_4O_{10}(OH)_2}]\text{per half unit cell}, \tag{1.1}$$

where x is the proportion of Li-ions per half unit cell. The first set of brackets denotes the guest layer where M refers to a generic monovalent interlayer cation and $\mathrm{nH_2O}$ refers to the discrete number of water layers. The second set of brackets denotes the host layer [8].

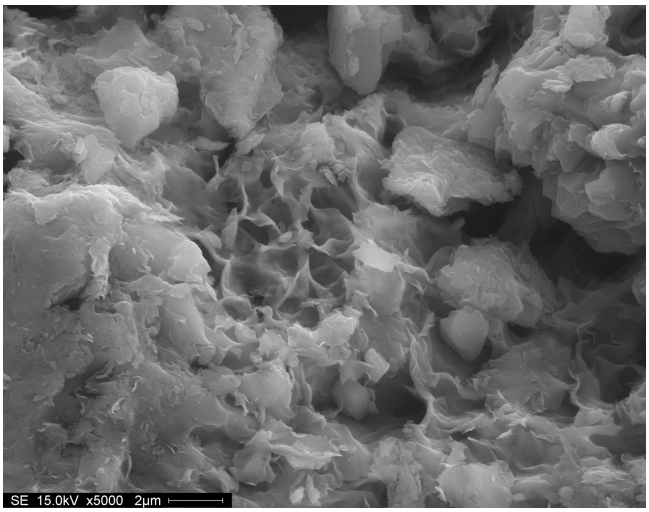

Figure 1.4: A SEM image of Hectorite SHCa-1 showing typical hectorite morphology.

Sodium fluorohectorite (NaFh)

In NaFh the hydroxyls in the hectorite formula (1.1) is replaced by fluorine ions (F^-) and the interlayer cation is sodium (Na). This results in the NaFh formula

$$[Na_x \times nH_2O][(Mg_{3-x}Li_x)Si_4O_{10}F_2]. \tag{1.2}$$

NaFh represents an extreme in both particle size and layer charge compared to other smectite clays, with a particle/grain size of up to 20 000 Å and a layer charge of $1.2\,e^-$ per unit cell [13]. A single particle/grain consists of 80-100 platelets on average [2]. The NaFh structure has three stable hydration states consisting of 0, 1 or 2 monolayers of water (0WL, 1WL and 2WL), and are quite well ordered along the stacking direction. The mean basal spacing of the three hydration states are 10 Å (0WL), 12 Å (1WL) and 15 Å (2WL) respectively [2]. However, there can be changes of $\sim$0.3 Å in the basal spacing also within the different hydration states dependent on the relative humidity [1].

1.2 Carbon dioxide (CO_2)

CO_2 is a colorless and ordorless gas which is found throughout nature and is the primary component of exhaled air of all animals. Although many maybe know it best as the gas used to make the bubbles in soft drinks, it is also the product of oxidation of all carbonaceous matter and an end product of complete combustion [14]. CO_2 is a greenhouse gas which makes it one of the gases that greatly effects the temperature on the Earth's surface. The reduction of the human-caused increase of athmospheric CO_2 has been of high interest the last decade, seen for example by the attention from the UN [15], because of the damaging effect it has on the earths climate. The interest, has among other things set a focus on the technology regarding methods of carbon capture and sequestration [16].

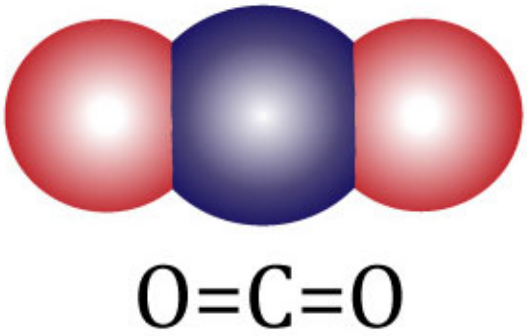

Figure 1.5: The CO_2 is a linear molecule with a central carbon atom doubly bound to two oxygen atoms.

Chemical and Physical Properties

Carbon dioxide is a linear molecule which is composed of a central carbon atom forming double covalent bonds to two Oxygen atoms. The chemical structure is hence O=C=O. Its linearity, the angle of 180° between the oxygen and carbon atoms, maintains a zero net dipole moment. In figure 1.6, which shows a pressure-temperature phase diagram of CO_2, one sees that CO_2 can be found in three different phases: gas/vapor, liquid and solid. In the gaseous state at atmospheric pressure the CO_2 is 1.53 times heavier than air, with a density of 1.80 g/L at 25°C. CO_2 has a triple point, which is found at the temperature -56.6°C and at 5.19 bar pressure. In the solid state, commonly known as dry-ice, the CO_2 forms as white snow-like flakes. The transition into dry ice occurs at -79°C at atmospheric pressure, and because of this low temperature, CO_2 in the solid state is commonly used as a cooling agent [14].

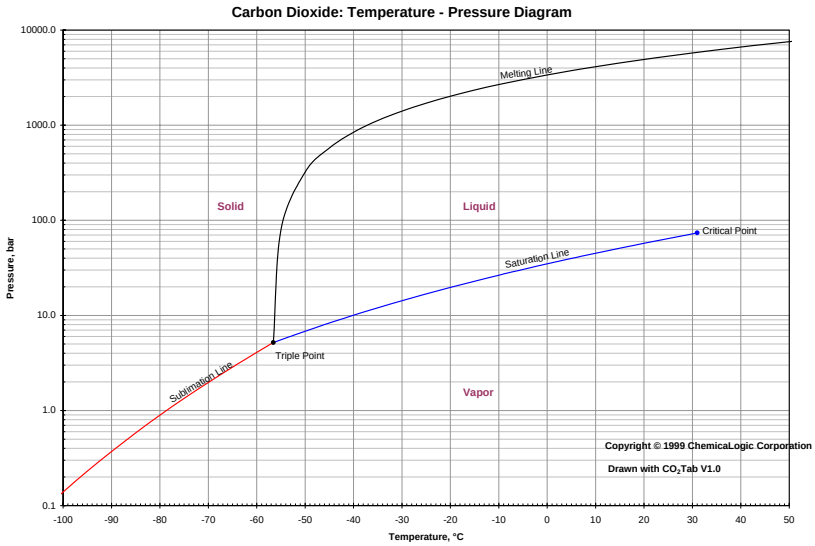

Figure 1.6: Temperature-Pressure phase diagram for CO_2. CO_2 exists in three states; solid, liquid and gas/vapor. The temperature is given in degrees Celsius and the pressure in log bar.

When in a double bond, carbon has the radius of 0.67 Å while oxygen has a radius of 0.57 Å [17], making the approximate length of the CO_2 molecule 3.6 Å(measuring along the long axis) and a maximum height of 1.3 Å (diameter of the carbon atom).

1.3 X-ray Diffraction

X-ray diffraction is an excellent, and also one of the most common, methods for the investigation and determination of structure for many materials. The phenomenon of diffraction of X-rays in crystals was first discovered by Max von Laue in 1912. In the work, for which he received the Nobel Prize in Physics for 1914 [18], he described the physics and derived a mathematical formulation of the interaction between X-ray photons and electrons in a crystal sample. By doing so, he managed to explain the remarkable scattering patterns that had been observed [19].

What will be described in the next sections is the kinematical approximation, for which the scattering is considered so weak that multiple scattering effects can be neglected.

Scattering from a electron

X-rays scatters from electrons in a sample. Although complex systems of molecules or a clay powder usually have a characteristic structure and form, a good staring point for introducing scattering theory is first to look at the scattering from the structureless electron. When an electron is placed in an electric field from an incident X-ray beam with wave vector $\mathbf{k}$, it is forced to oscillate with the field. The vibrating electron then acts as a source emitting radiation with the same frequency (assuming elastic scattering, *Thomson scattering*) as the incident radiation. From the Maxwell's equations one can derive expression of the radiated field at a distance R away from the electron, and hence also a relation between the incident and radiated field [20]

$$\frac{E_{rad}(R)}{E_{in}} = -r_0 \frac{e^{ikR}}{R} \cos\psi. \tag{1.3}$$

Here

$$r_0 = \frac{e^2}{4\pi\epsilon_0 mc^2} = 2.82 \times 10^{-5}\ \text{Å} \tag{1.4}$$

is known as the classical electron radius or the *Thomson scattering length*. In equation 1.3, the factor of $\cos\psi$ has been multiplied to obtain the oscillation that is observed at a certain position $X(R, \psi)$. The polarization of the incident X-ray beam determines how the electron oscillates. How much of this oscillation that is observed, depends on which plane the observation point is in compared to the polarization. An illustration showing the relationship between the incident wave, the scattering electron and the point of observation is found in figure 1.7.

The ratio between the incident and radiated field leads to an expression for the *differential cross section*. This term is defined as the number of photons scattered per second into a solid angle $d\Omega$, divided by the incident flux times

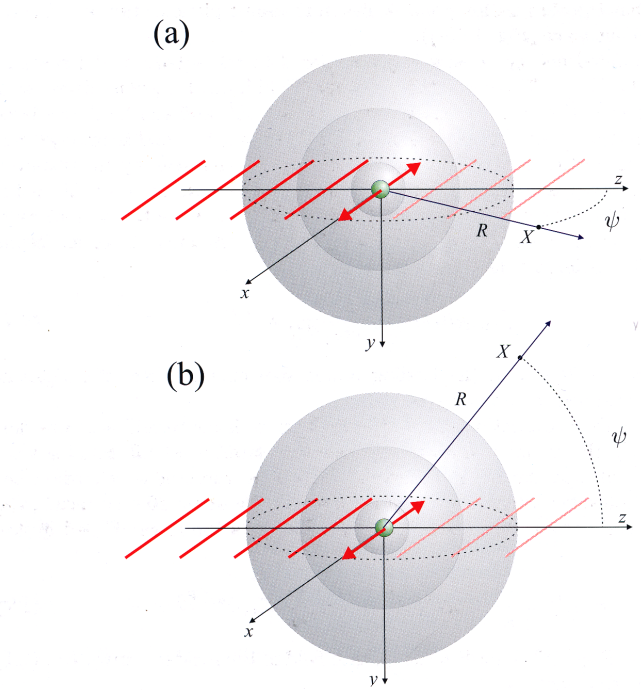

Figure 1.7: The classical description of the scattering of an X-ray by an electron. The incident plane wave is propagating along the z-axis and is polarized along the x-axis. In (a), the observation point X lies in the same plane as the polarization and the observed oscillation is obtained through the multiplication of the factor $\cos\psi$. In (b) the observation point lies in the plane perpendicular to the polarization and the full oscillation is seen at all scattering angles ψ. Adapted from [20].

the same solid angle. The differential cross section for Thomson scattering is

$$\frac{d\sigma}{d\Omega} = r_0^2 P \tag{1.5}$$

for which the polarization factor P depends on the polarization of the incident radiation.

$$P = \begin{cases} 1 & \text{synchrotron: vertical scattering plane} \\ \cos^2\psi & \text{synchrotron: horizontal scattering plane} \\ \frac{1}{2}(1+\cos^2\psi) & \text{unpolarized source} \end{cases}$$

[20].

Scattering from an atom

In an atom there are one or more scatterers moving about a center. Since electrons are identical particles, it is convenient to introduce a charge distribution function $\rho(r)$, to better describe what the incident X-ray beam encounters. $\rho(r)$ is defined as the density of electrons for an atom at a distance r away from the mass center. The distribution leads the concept of the *atomic form factor*, which is given as the Fourier transform of $\rho(r)$,

$$f(\mathbf{Q}) = \int \rho(\mathbf{r}) e^{i\mathbf{Q}\mathbf{r}} d\mathbf{r}. \tag{1.6}$$

In the equation above, $\mathbf{Q}$ is the scattering vector given by the difference between incident and scattered wavevector $\mathbf{Q} = \mathbf{k} - \mathbf{k_{sc}}$ (see figure 1.9 b). The form factor is describing the scattering power of the atom, and in the forward direction ($\mathbf{Q} = 0$) the form factor is equal to the atomic number Z. The intensity, which is the observable, relates to the form factor by that it is proportional to its absolute square $|f(\mathbf{Q})|^2$. By taking the absolute square, the imaginary part of equation 1.6, the phase factor, is lost [20]. The phase is therefor not measurable and it is thus not possible to obtain the charge distribution directly from the Fourier transform of the intensity.

Mathematical, the Fourier transformation is a very important tool in scattering theory. It provides the mathematical relationship between the morphology of the structure under investigation, and the scattering patterns that are observed.

Scattering from an unit cell

As each atom has a form factor, it is possible to calculate an *unit cell structure factor*, F_{str}, when the atoms are placed in certain positions to form a unit cell. The unit cell structure factor accounts for the difference in scattering power from the individual atoms. It also includes the phase differences that arises from the spatial distribution within the unit cell. By labeling the different atoms in the unit cell by index j and knowing the position and form factor of the individual atoms one can write

$$F_{str}(\mathbf{Q}) = \sum_j f_j(\mathbf{Q}) e^{i\mathbf{Q}\mathbf{r_j}} \cdot e^{-M_j}. \tag{1.7}$$

Here M_j is the Debye-Waller factor and accounts for the reduction of intensity caused by thermal acoustic vibrations. In a compound each type of atom will have a different Debye-Waller factor, since in general light atoms vibrate more easily than heavy atoms [20]. It is not given that all the positions of the atoms in the unit cell are known, and it is hence not always straight forward to calculate the unit cell structure factor.

Scattering from a layered clay

The unit cell structure factor (eq.1.7) is defined by the discrete indices *hkl* and is hence not a continuous function in Q. As clays are described as a composition of layers, they can in many ways be considered one dimensional. A transformation from a discrete to a continuous structure factor is thus possible and quite straight forward. If considering a centrosymmetric system one can simply define a *layer structure factor* $G(Q)$ as [21]

$$G(Q) = \sum_j n_j f_j(Q) \cos(Q z_j) \cdot e^{-M_j}. \tag{1.8}$$

Here n_j is the number of atoms of type j located at a distance z_j away from the origin of the system. The above equation for $G(Q)$ is clearly continuous in Q.

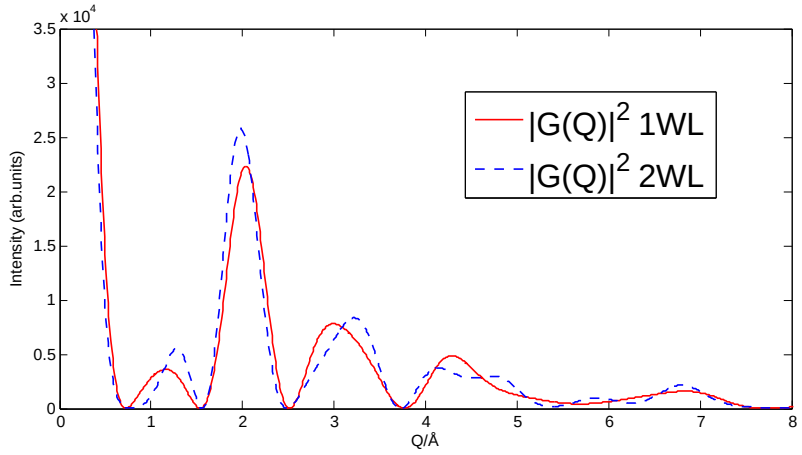

Figure 1.8: A mathematical computation of the squared layer structure factor $G(Q)$ for the NaFh in the 1WL and 2WL hydration state, based on tabulated values for the different atomic form factors. The intercalated water changes the layered structure factor and hence the diffraction pattern.

Bragg's law of diffraction

The defining property of a crystalline material is its periodicity or long range order [22]. Elementary treatments of scattering of X-rays from a crystal lattice leads to Bragg's law which is expressed as

$$2d_{hkl} \sin(\theta) = n\lambda \tag{1.9}$$

and is the condition for the constructive interference between waves with an angle of incidence θ, the Bragg angle, to a set of adjacent lattice planes a

distance d_{hkl} apart [23]. When using a single wavelength, which is the case in X-ray diffraction, the Bragg equation is typically expressed with $n = 1$. Although Bragg's law explains many of the diffraction phenomena, it is mearly a simple geometrical interpretation of diffraction by a crystal. When dealing with X-rays it is often more convenient to use the original formalism, based on a pure physical platform, which followed from the discovery of diffraction by Max von Laue [19].

Reciprocal space and the Laue formalism

What might already be evident is that there is an inverse relationship between the structure and form of the scatterer in real space, and the resulting pattern which is observed. The concept of *reciprocal space* was introduced by P. P. Ewald in 1921 [24] as a tool to both illustrate and understand this relationship. In this concept, the connection is through the Fourier transform, which takes us from real space to reciprocal space, or vice versa. As an example, the already mentioned scattering vector $\mathbf{Q}$ is a vector in reciprocal space. If one defines the shape and size of the unit cell in real space with vectors, $\mathbf{a}, \mathbf{b}$ and $\mathbf{c}$, these vectors have their corresponding reciprocal lattice vectors, $\mathbf{a}^*, \mathbf{b}^*$ and $\mathbf{c}^*$. The reciprocal vectors then satisfies the condition

$$\mathbf{a} \cdot \mathbf{a}^* = \mathbf{b} \cdot \mathbf{b}^* = \mathbf{c} \cdot \mathbf{c}^* = 2\pi \tag{1.10}$$

and

$$\mathbf{a}^* \cdot \mathbf{b} = \mathbf{a}^* \cdot \mathbf{c} = \mathbf{b}^* \cdot \mathbf{a} = \mathbf{b}^* \cdot \mathbf{c} = \mathbf{c}^* \cdot \mathbf{a} = \mathbf{c}^* \cdot \mathbf{b} = 0. \tag{1.11}$$

The distance between two scatterers in a real space three-dimensional lattice are expressed with the translation vector

$$\mathbf{R}_{uvw} = u\mathbf{a} + v\mathbf{b} + w\mathbf{c}, \tag{1.12}$$

where u,v and w are integers refering to lattice points. The reciprocal vector corresponding to this real space vector is termed the *reciprocal lattice vector*

$$\mathbf{G}_{hkl} = h\mathbf{a}^* + k\mathbf{b}^* + l\mathbf{c}^*, \tag{1.13}$$

where hkl are the miller indices. This vector defines the allowed directions of the scattering. The reciprocal equivalent to Bragg's law is the Laue condition which is fulfilled when the scattering vector $\mathbf{Q}$ is equal to $\mathbf{G}_{hkl}$.

$$\mathbf{Q} = \mathbf{G}_{hkl} = 2\pi \frac{\hat{\mathbf{n}}_{\mathrm{hkl}}}{d_{\mathrm{hkl}}}. \tag{1.14}$$

Compared to equation 1.13 this equation describes the crystal structure in terms of crystal planes that have a interplanar spacing $\mathrm{d_{hkl}}$ apart, instead of atomic positions. The vector $\hat{\mathbf{n}}_{\mathrm{hkl}}$ is a unit vector normal to the plane (hkl).

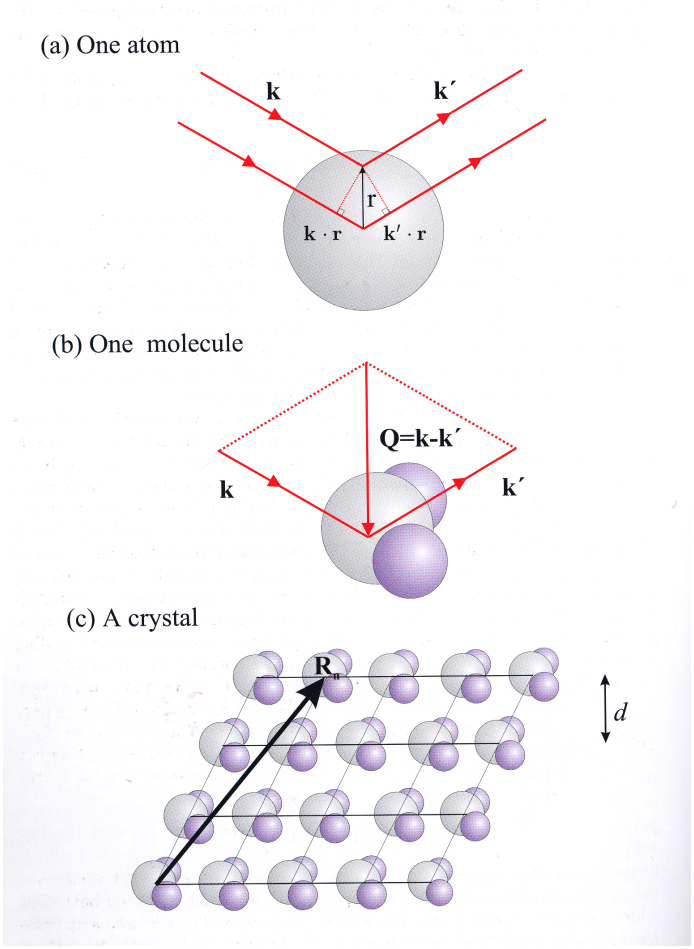

Figure 1.9: Scattering from an atom (a), a molecule (b) and a crystal (c). An atom is represented by a electron density distribution where the difference between scatterers inside gives rise to a phase difference between the incident and radiated field. The scattering vector **Q** is defined as the difference between the two wave vectors **k** and **k**′. In a ideal crystal each molecule or unit cell are positioned in certain fixed positions which can be expressed by the translation vector **R**. The long range order and translational symmetry that this implies cause interference effects. Adapted from [20].

As Bragg's law, the condition represents a big limitation of the scattering from a crystal and yield a selection rule [22]. When summing up this selection rule from an assemblage of cells one ends up with what is termed the *interference function*

$$S(\mathbf{Q}) = \sum_{hkl \neq 000} \delta(\mathbf{Q} - \mathbf{G}_{hkl}) \tag{1.15}$$

for an ideal crystal, which describes the interference as a function of the scattering vector $\mathbf{Q}$. As was the case with the unit cell structure factor, this is also a discrete function given by the miller indices hkl. When transforming it into a continuous function one gets [21]

$$S_{lc}(Q) = \sum_{N=n_1}^{N=n_2} p(N) \frac{\sin^2(QNd/2)}{\sin^2(Qd/2)}. \tag{1.16}$$

Since the the crystalites can vary in size the term $p(N)$ is introduced and is the proportion of crystallites for the number of unit cells N stacked in the direction perpendicular to the layers.

Lorentz-polarization factor

The *Lorentz-polarization factor* $L_p(Q)$ is a important experimental quantity that control X-ray intensity with respect to diffraction angle. The factor is a combination of the polarization factor P (see section 1.3) and the Lorentz factor[2] L. The Lorentz-polarization factor is given by

$$L_p = \frac{P\psi}{\sin(2\theta)}. \tag{1.17}$$

The equation yields that the Lorentz factor is an combination of two geometrical factors. ψ is the powder ring distribution factor and accounts for the number of crystals favorably oriented for diffraction at any Bragg angle, while $\sin(2\theta)$ describes the irradiated volume of a crystal as a function of 2θ. For a random powder, ψ is proportional to $1/\sin(\theta)$ while it is constant for a single crystal [25]. In the case of clay minerals ψ is somewhere in between the two limiting cases [21].

Powder diffraction

An ideal crystalline powder consists of many thousands of tiny crystallites randomly orientation. This means that direction of the reciprocal lattice vectors $\mathbf{G}_{hkl}$ are isotropically distributed. This random orientation secures that a fraction of the crystallites always fulfills the Laue condition, so no rotation is needed

[2] This factor should not be confused with the factor of the same name that appears in several equations in special relativity.

to observe the diffraction. Each *hkl*-reflection represents a cone with an axis that lies on the direction of the incident X-ray and has an apex half angle of 2θ. This cone is often referred to as the Debye-Scherrer cone, named after the physicists that first developed the method of analysis of powder diffraction [20].

Diffraction from a clay powder

Taking in account all the factor mentioned above, the measured intensity at scattering experiments with clay powder should appear as this:

$$I(Q) = |G(Q)|^2 S_{lc}(Q) L_p(Q). \tag{1.18}$$

A layered clay is like other minerals, characterized by one type of unit cell. The types of atoms and the position of them in the cell will contribute to the layer structure factor. As mentioned in section 1.1.1 the distances between the stacked planes, the basal spacing d_{001}, is describing the features of the geometry of the unit cell and the stacking of the layers. This will be the cause of the repeated interference pattern observed, which is represented in formula by the interference function. The diffraction pattern will take the shape of a cone because of the isotropic distribution of the clay particles in a powder. The intercalation of any guest substances in clays are indicated by the unit cell incorporating more atoms and that the d_{001}-spacing changes. This will affect both the layer structure factor and the interference function, and can thus be observable with the use of X-ray powder diffraction.

Diffraction Peaks

Peak shape and breadth may become important part of diffraction analysis in the future, but still most analysis of clay minerals are based on peak position and intensity [21]. For the analysis of diffraction patterns, it is in any case favorable to describe the peaks as good as possible.

Pseudo-Voigt approximation

It has been shown that x-ray diffraction peak shapes are very well described by the pseudo-Voigt function [26]. The pseudo-Voigt function is a simple approximation to the Voigt function, which again is a convolution of a Gaussian

$$f_G = \frac{1}{\sigma\sqrt{2\pi}} e^{-\frac{(x-\mu)^2}{2\sigma^2}} \tag{1.19}$$

and a Lorentzian

$$f_L = \frac{1}{\pi} \frac{\omega}{(x - x_c)^2 + \omega^2} \tag{1.20}$$

function. In the the Gaussian function, also known as the normal distribution, the μ is the mean and σ is the standard deviation. In the Lorentzian function

the parameters x_c and ω is a specifying the location of the peak and half-width at half maximum(HWHM), respectively. A convolution is widely significant as a physical concept and is a mathematical operator which takes two functions, $f(x)$ and $g(x)$ and produces a new function $h(x)$ defined by the integral

$$h(x) = \int_{-\infty}^{\infty} f(u)g(x-u)du \tag{1.21}$$

or briefly $h(x) = f(x) \otimes g(x)$. In a sense it describes the amount of overlap when the one function is sweeped over the other moving from minus to plus infinity. A convolution is also a commutative operation so $f(x) \otimes g(x) = g(x) \otimes f(x)$ [27]. The voigtian function then becomes

$$f_V(x; \mu, \sigma, x_c, \omega) = \int_{-\infty}^{\infty} f_G(u; \mu, \sigma) f_L(x-u; x_c, \omega)du. \tag{1.22}$$

However, an analytical form of this function is not available, and the pseudo-Voigt function is a simple approximation to the Voigt function which is much more convenient from the programming point of view [26]. There are two types of pseudo-Voigt functions, one where the Gaussian and Lorentzian distributions have different full width at half maximums (FWHMs), and one where the FWHMs are equal.

$$f_V(x; x_c, \omega) = (1-\eta) f_G(x; x_c, \omega) + \eta f_L(x; x_c, \omega). \tag{1.23}$$

Equation 1.23 describes the pseudo-Voigt function where the FWHMs are the same of the Gaussian and Lorentzian distribution. The parameter η is the shape parameter, which describe the amount of contribution from each of the distributions. A shape factor of zero is a pure Gaussian, while a shape factor of one is a pure Lorentzian. It has been proved that this pseudo-Voigt type provides an approximation accurate to about 99% of the real Voigt profile. The shape factor allows one to easly shift between the two contribution from the two functions, depending on which effects is determening the peak shape. When lifetime effects are important, the contribution from the Lorentzian is the dominant. The Gaussian on the other hand, contributes most when instrumental or random statistical effects are most important [28].

Hendricks-Teller state

As described in section 1.1.2 swelling clays are characterized by beeing able to incorporate guest substances between the nano layers of clay, leading to different intercalated states. The different intercalation states lead to defined diffraction peaks that can be well profiled by the pseudo-Voigt function described above. There are however, in the transition between two intercalation states, mixed intercalation states known as the Hendricks-Teller state [2], named after the physicists that first described the X-ray interference from partly ordered layer lattices [29]. This state originates from the fact that the transition is a dynamic

transition, and that there can be a two-state coexistence. In the diffraction pattern, this state is seen by different maxima emerging and leading to a broad distribution in-between peaks. The position of this distribution is dependent on the fraction of particles that are in the different intercalation states. The Hendricks-Teller state has been reported in many studies regarding hydration transitions in clay [1, 2, 3, 4].

1.4 X-ray sources

The sources and methods of generating X-rays for structural investigation has come a long way since the discovery of the X-ray in 1895 by Wilhelm C. Röntgen and the phenomenon of X-ray diffraction by crystals by Max von Laue in 1912 [23]. The type of X-ray generating source one uses is of high importance, in an experiment, and if one wants to utilize the theory presented above. Because the source determines the probe, X-rays with a certain wavelength, with which you investigate, it greatly limits how much and how well you can 'see' with the X-rays. Two types of generating sources and the physics behind them will be presented in this section: the *Electron impact*, which is a laboratory source of X-rays, and *Synchrotron* which is a large scale cyclic particle accelerator.

1.4.1 Electron impact source

Electron impact in X-ray tubes is the most common laboratory source of X-rays. X-ray tubes contain a high voltage power source, which is connected across a cathodic filament and an anode, both confined in a high vacuum chamber. When a voltage difference is set by the power source, the cathode filament constantly emits electrons that are collected by the anode. The electrons collide with the anode with such a power that they accelerate other electrons, ions and nuclei within the anode material. This collision energy results in emission/radiation of X-ray photons. The radiated spectrum (see figure 1.10) is composed of *Bremsstrahlung*, which are produced by the rapid de-acceleration of the electrons when colliding with a solid target, and *characteristic radiation*. The characteristic radiation is produced when the exited hole in a target atom, which arises as a result of the electron impact ionization, is relaxed by an outer electron falling to fill this vacancy[30]. The intense bombardment of the anode

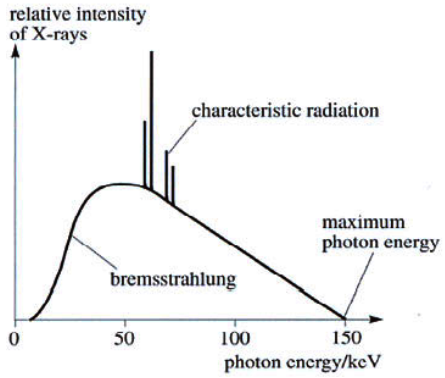

Figure 1.10: Radiation spectrum from a x-ray tube. The Bremsstrahlung is seen as a broad distribution, whereas the characteristic radiation is seen as sharp peaks in the radiated spectrum.

by electrons creates a large amount of heat within the anode. The efficiency of the X-ray generation is less than 1%, where the remaining energy is lost as heat [30]. The cooling down of the anode, usually by water, is therefore an important part in the process of the electron impact X-ray generation.

1.4.2 Synchrotrons

In the 1970 it was realized that the radiation emitted from charged particles circulating in storage rings, originally constructed for high energy nuclear physics experiments, had the potential to be a much more intense and versatile source of X-rays than the sources available at that time. This discovery lead to the construction of storage rings dedicated solely to this purpose. These storage rings are today called synchrotrons and the radiation they provide is called synchrotron radiation [20].

Synchrotron radiation

Electrons emit radiation when accelerated, which is a direct consequence of the finite velocity of light. During acceleration the electric field close to the electron is required to rearrange and this field perturbation is what is observed as electromagnetic radiation [31]. The power, S, radiated by a electron with a speed, v, is given by the Larmor formula

$$S = \frac{2}{3}\frac{r_0}{m_e c}\left|\frac{d\mathbf{p}}{dt}\right|^2, \tag{1.24}$$

where m_e is the mass of the electron, c the speed of light, r_0 the classical electron radius and $\mathbf{p}$ the electron momentum. The Lorentz formula

$$\left|\frac{d\mathbf{p}}{dt}\right| = e(\mathbf{E} + \mathbf{v} \times \mathbf{B}) \tag{1.25}$$

contains the acceleration and describes the motion of an electron in an electric, $\mathbf{E}$, and a magnetic, $\mathbf{B}$, field. This is the general formula that apply when the speed of the electron is much less than c. However in synchrotrons, highly relativistic electrons are used. One then has to use the relativistic invariant form of equation 1.24 obtained through replacing $d\mathbf{p}/dt$ with the relativistically invariant quantity $d\mathbf{P}/d\tau$, which relates through

$$\left|\frac{d\mathbf{P}}{d\tau}\right|^2 = \left|\frac{d\mathbf{p}}{d\tau}\right|^2 + \frac{1}{c^2}\left(\frac{dE}{d\tau}\right)^2. \tag{1.26}$$

Th Larmor formula is then expressed as

$$S = \frac{2}{3}\frac{r_0}{m_e c}\left|\frac{d\mathbf{P}}{d\tau}\right|^2. \tag{1.27}$$

Equations 1.26 and 1.27 are given in the reference frame where the electron is at rest, the relation to the laboratory frame is through the Lorentz factor $\lambda = (1 - v^2/c^2)^{-1/2}$

$$\frac{d\mathbf{P}}{dt} = \frac{1}{\lambda}\frac{d\mathbf{P}}{d\tau}. \tag{1.28}$$

Because the electrons radiate energy, the energy of the electron, E, and $\mathbf{p}$ are changing and $d\mathbf{p}/dt$ has two components, $p\omega = pv/R$, where ω and R are the angular velocity and radius of the orbit, respectively. Because of $v \approx c$ and hence $m_e c^2 \ll E$, the momentum p equals E/c so that equation 1.27 can be simplified to [30]

$$S = \frac{e^2 c}{6\pi\epsilon_0}\frac{1}{(m_e c^2)^4}\frac{E^4}{R}. \tag{1.29}$$

When electrons are subjected to an acceleration perpendicular to their direction of motion, they start to move in curved paths. Since the velocity of the electrons is close to the speed of light, the radiation appears to be emitted in the general direction of motion and the pattern is folded into a sharp cone. An illustration of this is found in figure 1.11. The angle with which the cone appears in the laboratory, is approximately equal to the inverse Lorentz factor, $1/\lambda$. The abil-

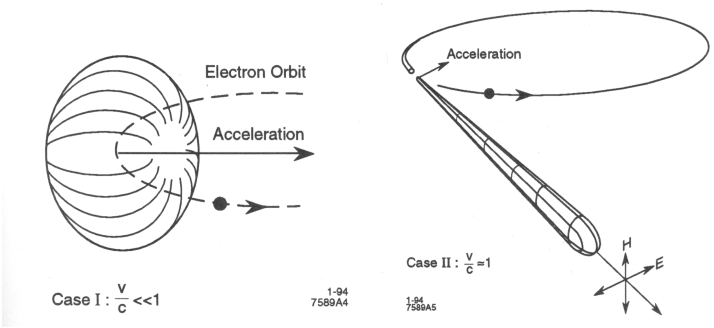

Figure 1.11: Accelerated electrons at a low velocity (Case I) radiate in a rather non-directional pattern, whereas radiation from accelerating electrons approaching the speed of light (Case II) is concentrated into a small cone around the forward direction. Adapted from [32].

ity of the storage ring to generate this narrow cone of radiation, has created the concept of brilliance, which is widely used in the synchrotron radiation community. The brilliance is the number of emitted photons per second in a narrow energy bandwidth (BW) per unit solid angle. This can then be written as [33]

$$\text{Brilliance} = \frac{N_{\text{photons}}}{\sigma_x \sigma_y \sigma_z \sigma_x^t \sigma_y^t \text{BW}} \tag{1.30}$$

where $\sigma_x\sigma_y\sigma_z$ are the spatial divergence and $\sigma_x^t\sigma_y^t$ are the source angular divergence. The synchrotron radiation, for which the physics has been described here, can range from infrared (IR) to Hard X-rays (HXR) and therefore attracts a variety of scientific fields.

Storage rings and insertion devices

The synchrotron storage ring is the arrangement of components that enables the electrons to circulate at velocities close to the speed of light, for periods of several hours, while emitting synchrotron radiation. To preserve the characteristics of the synchrotron radiation, and transport the beam to the experimental end stations, *beamlines* are positioned in tangential lines from the storage ring. A beamline can be divided into three parts which can be present altogether or just one or two of them. *Prefocusing* is the first part that the radiation encounters and there the characteristics of the beam are adapted to meet the needs of the following section, the *monochromator*. The monochromator selects the particular wavelength that is provided. The last part is the *refocusing* which adapts the beam dimension or divergens to the individual experiments [33].

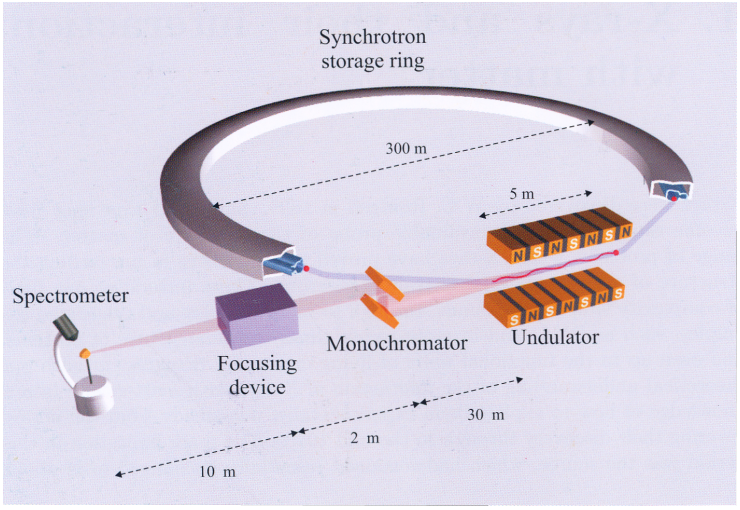

Figure 1.12: Synchrotrons are large storage rings which enables relativistic particles to circulate in a closed orbit emitting synchrotron radiation. Insertion devices such as the undulator can be found in third generation storage rings and are placed in straight magnet free section in the synchrotron. The undulator provides the radiation to the beam line that are found along the tangential of the synchrotron storage ring. The beamlines consists of focusing devices and monochromators that alters the beam to meet the need of the individual experiments. Adapted from [20].

The first synchrotrons were actually designed for high energy physics, and were first handed over to the synchrotron radiation community when the original usefulness of the ring was exhausted. Those types are now known as first generation storage rings. The first rings designed as dedicated light sources are named second generation storage rings. These are characterized by having more beamlines and experimental stations than the first generation. The third generation storage rings are distinguished by lower electron-beam emittance, and by straight magnet free section with insertion devices. The beamlines at third generation storage rings are often also each optimized for a particular kind of research [32].

Bending magnet Bending magnets are used to deflect the electron beam and guide the electron in a approximately circular orbit in the storage ring and the emitted radiation has a continuous energy spectrum. The sharp cone of radiation is linearly polarized with the electric field parallel to the plane of orbit and sweeps around the storage ring like a well-focused search light. The synchrotron radiation emitted from the bending magnets does not nesceceraly meet the requirements of the user. Therefor insertion devices are placed in between the bending magnets to provide the desired radiation characteristics [30, 32].

Wiggler The output of a storage ring can be significantly enhanced with the use of insertion devices. A wiggler magnet is a succession of magnetic poles with alternating polarity and is used to produce high intensity broad band radiation which greatly exceeds the radiation from bending magnets. The spectrum from a wiggler is the same as that from a bending magnet of the same field strength. A wiggler magnet is designed in such a way that the alternating deflections are canceled out, and no net bending is produced [32].

Undulator An undulator magnet is similar to a wiggler in the way that it also is a succession of alternating magnetic poles. However, in a undulator, the radiation emitted at one oscillation is in phase with the radiation from the following oscillations. In terms of brilliance the undulators are some order of magnitude higher than the bending magnets [33]. In figure 1.13 a comparison of the emission patterns are shown, while a comparison of the typical energy spectra of a wiggler and an undulator is found in figure 1.14.

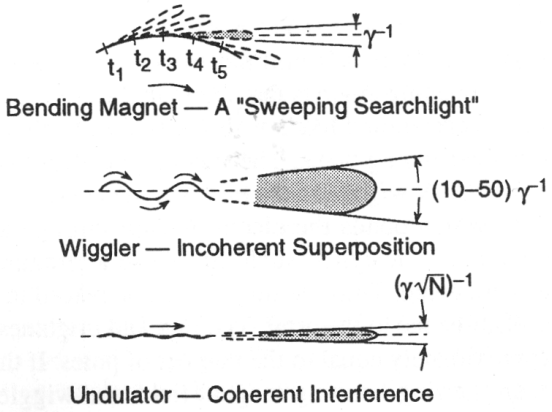

Figure 1.13: A graphical description of the emission patterns from bending magnets, wiggler magnets and undulator magnets. Adapted from [32].

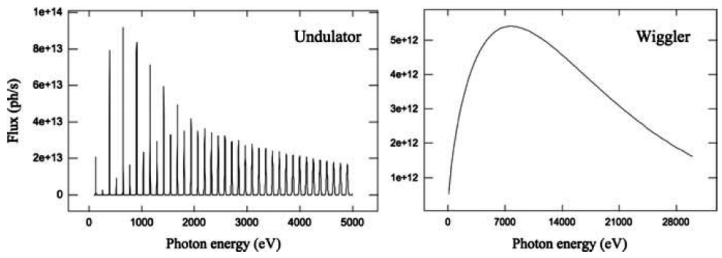

Figure 1.14: A comparison of typical energy spectra emitted from an undulator (left) and a wiggler (right) collected after a beam defining aparature. The y-axis show the flux, photons per second, and the x-axis the energy in electron volts (eV). Adapted from [33].

Chapter 2

CO_2 Intercalation Experiment

2.1 Experimental setup

The X-ray scattering measurements I have performed and which make up the basis for the 'CO_2 Intercalation Experiment' were conducted at the crystallography beamline I711 at the MAXII synchrotron radiation facility in Lund Sweden, and at Norwegian University of Science and Technology (NTNU) with the use of the NanoStar from Bruker AXS. The experiment conducted at MAX-lab were performed from the 14th to the 17th of February 2011.

2.1.1 MAX II Beamline I711

The MAXII is a 3rd generation storage ring and the crystallography beamline I711 is used for single crystal diffraction (macromolecular as well as small molecule), powder diffraction and small angle x-ray scattering (SAXS). The X-ray source is a multi-pole wiggler which can provide x-ray wavelengths in the range from 0.95 Å to 1.4 Å. For this experiment the wavelength was set to 1.2 Å. The monochromator is a single asymmetrically cut Si(111) crystal, bendable for horizontal focusing, and with a horizontal diffraction plane. The station is currently equipped with a ADSC 210 area CCD detector [34].

2.1.2 NanoStar Bruker SAXS

The NanoStar is a small angle X-ray scattering instrument which is used to study structures ranging from some nanometers, i.e. wide angle scattering (WAXS), to several hundreds of nanometers, i.e. small angle scattering (SAXS). The instrument is composed of four main parts: a generating source with mirror optics, a pinhole collimating system, a sample chamber and a 2D detector. The generating source is an electron impact source with a copper anode producing

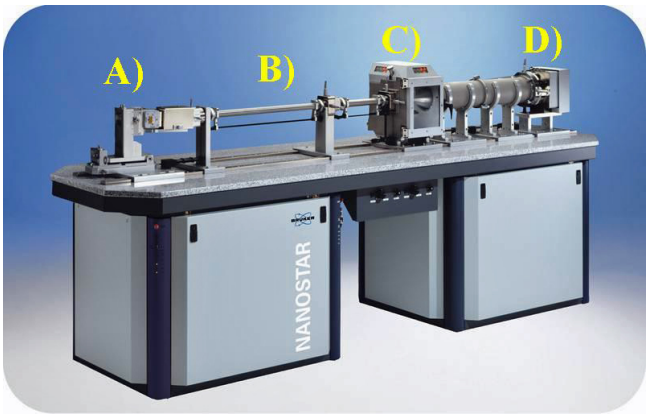

Figure 2.1: Photograph of the NanoStar harware in the SAXS setup. A) Generating source B) Pinhole collimating system C) Sample chamber D) Detector. Adapted from the Bruker webpage.

K_{alpha}-radiation. The detector, Histar, is a 2D multiwire grid detector that uses pressurized xenon gas to sense and determine the x- and y-position of the X-rays. Technical data of the Nanostar is found in table 2.1 and a picture of the instrument, showing all its components, can be found in figure 2.1.

Technical data - Nanostar Bruker SAXS	
Filament	$0.5\,\text{mm} \times 0.5\,\text{mm}$
Wavelength λ	$1.541\,838\,\text{Å}$
Beam diameter	$400\,\mu\text{m}$
Minimum sample-to-detector distance	110 mm
Maximum sample-to-detector distance	1070 mm
Detector diameter	10.5 cm
Detector resolution	1024×1024 Pixels
Size of pixels	horizontal and vertical 105.26 microns
Q-range	$\in [\sim 0.006\,28\,\text{Å}^{-1}, 2.79\,\text{Å}^{-1}]$

Table 2.1: Technical data for the Nanostar Bruker SAXS.

2.1.3 Sample holder

In order to carry out the experiment a new sample holder had to be custom made. This was done by the engineering workshop at NTNU. The sample holder consists of two parts, where one is bolt shaped and the other has the inverse shape, like a hollow cylinder. During the experiment the parts are screwed together. Both parts are made out of copper, which was chosen because of its good thermal conduction. The sample holder has a cylindrical shape with a

outer and inner diameter of 5 cm and 3 cm, respectively, and a length of 4 cm. It has an additional copper stem on the hollow part that secures a horizontal base. On each of the two parts there are 0.15 mm thick kapton windows[1] as the bolt shaped part contains the incident window, and the hollow part the exiting window. The front kapton window is glued onto the copper, covering a diameter of 1 mm, while the 6 mm diameter at the exiting side is covered by a kapton window that is pressed down by a threaded ring/disc. The backside has a conic shape to ensure that the surfaces does not interfere with the Bragg angles of interest. When the two parts are screwed together there is a distance of ~ 1 mm between the two kapton windows which make up the sample volume. To secure no leakage one O-ring is placed between the exiting kapton window and the copper while another is placed between the two copper parts. A technical drawing and a picture of the sample holder are shown in figure 2.2.

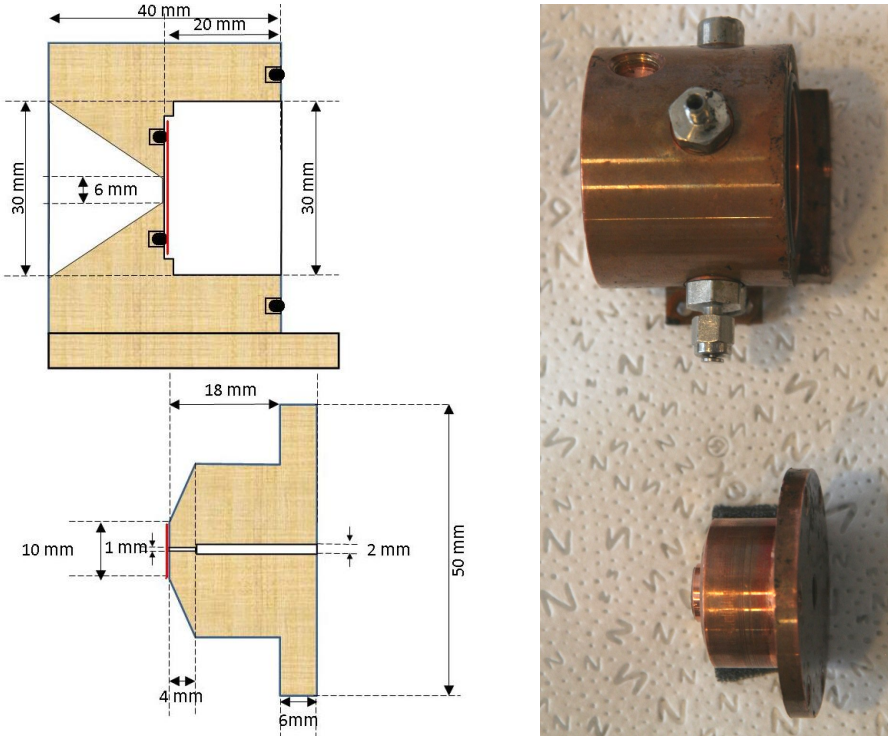

(a) (b)

Figure 2.2: A technical drawing (a) and the actual sample holder (b). The sample holder consist of one bolt shaped and one hollow part which are screwed together during experiments. On the hollow part there are connections to gas which leads directly into the sample volume.

[1]Kapton is a polyimide film with a high thermal and mechanical stability. This together with its high X-ray transmittance makes it a preferred option for X-ray windows.

The sample holder has two channels for connections to gas; one on the top and one on the left side of the hollow copper part. The channels lead directly into the sample volume. During experiments the gas connection on the top is used as the connection to the gas bottle, while the other is plugged. There are also two channels intentionally made for inserting and removing the clay samples[2]. The sample holder was designed to be able to withhold at least 15 bar pressure[3].

Cooling and isolation

To be able to regulate the temperature of the sample holder, the base was placed on a cooling system consisting of a temperature heat sink and peltier elements. The heat sink consisted of a copper bloc with channels for water flow connection. A circulator filled with anti-freeze was connected to the water flow channels and removed excess heat from the peltier elements. Since the peltier elements only gives a temperature difference with applied voltage, it is important to have one stable side to be able to vary the other as one wishes. Temperatures were set by adjusting the voltage over the peltier elements and by adjusting the temperature of the water bath. To avoid heat loss to the surroundings the sample holder was isolated, which was done by wrapping it in cork tape (tape made out of asphalt, rubber and cork).

Temperature and Pressure control and measurements

The temperature of the sample holder was measured with the use of a thermocouple. The thermocouple was inserted into a small hole that had been drilled into the stem of the sample holder. The temperature readout is thus only the temperature held by the copper at that position and one can expect a small error between this value and the actual temperature in the sample volume. This error is hence determined by thermal conductivity of the copper. The pressure was measured and controlled manually by the pressure regulator positioned on the tank. The regulator gives the pressure as pressure over atmospheric pressure.

2.1.4 Experimental setup at MAX-lab

The experimental setup at the I711 beam line consisted of the components mentioned above, but because of a different type of circulator provided at the MAX-lab, an improvised modification had to be done on the sample holder so that low temperatures could be reached. The solution to this problem was to drill a threaded hole on top of the sample holder. This hole allowed for a 'home-made' funnel, made out of copper and rubber tubes, to be screwed onto the sample holder (See figure 2.3 b)). When liquid nitrogen was poured into this funnel, it worked as a cold finger in thermal contact with the sample holder. Although it

[2]When changing sample, it was thus found easier and more convenient to screw the two parts apart than using these channels.

[3]The operational pressure range was not measured, but pressures up to 25 bar over ambient pressure could be maintained without damaging the cell.

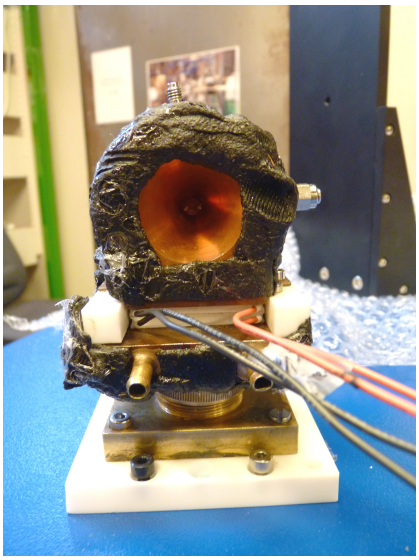

(a)

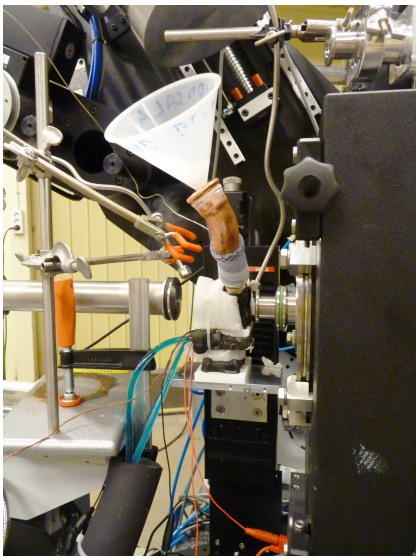

(b)

Figure 2.3: The sample holder was wrapped in cork tape to reduce heat loss to the surroundings and placed on top of the cooling system (a). The cooling system consisted of a copper bloc with channels with circulating water and peltier elements. At MAX-lab modification was made on the sample holder so that the cooling would be done more effectively (b). When liquid nitrogen was poured into the funnel, temperatures below -70° C was reached.

demanded continuous refilling to be able to keep stable temperatures, the device worked well and allowed us to reach the low temperatures (>-70°C) that was originally planed. To reduce the amount of frost on the sample holder windows, a flow of nitrogen was directed onto them. Figure 2.4 shows the experimental setup at MAX-lab.

2.1.5 Experimental setup at NTNU

The setup at NTNU was much alike that of the one used at MAX-lab. Instead of having a flow of nitrogen directed onto the kapton window, it was found sufficient to have silica gel inside the sample chamber. Since the sample chamber could be closed and sealed, the silica gel provided a low enough humidity so that little condensation or frost covered the kapton windows. Because the intensity of the NanoStar is significantly less than that from the I711-beamline, modifications were performed on the sample holder to minimize the sample volume and thickness.

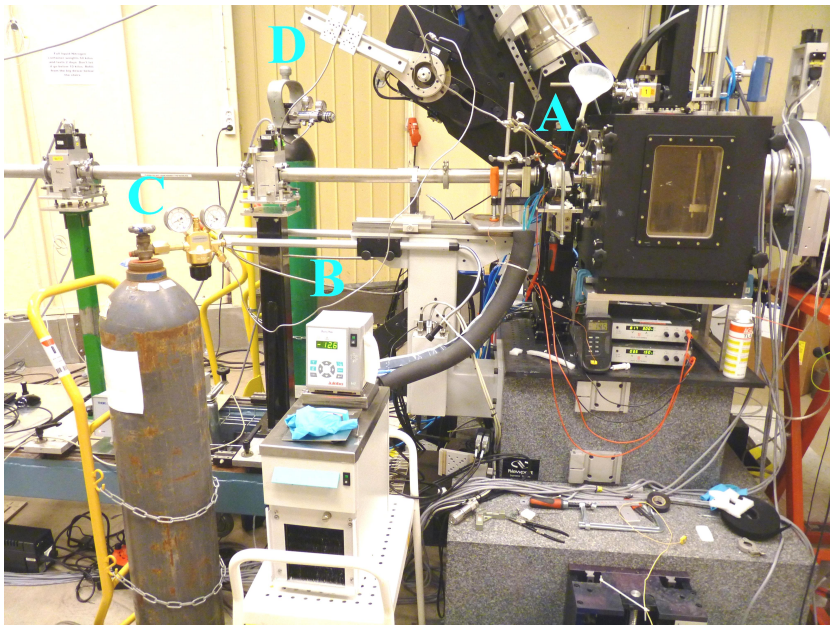

Figure 2.4: The experimental setup at MAX-lab. A) The sample holder positioned in the path of the X-ray beam B) Circulator providing a flow of anti-freeze to the hot side of the peltier elements. C) The pressure of CO_2 was set and read with the regulator positioned on the top of the gas bottle. D) Nitrogen was used to reduce the frost on the kapton windows.

2.2 Experimental method

2.2.1 Experiment at MAXII

Samples and preparation

The NaFh clay used in the experiment was purchased from Corning Inc. as pure Li-fluorohectorite and then subjected to a ion-exchange process in order to produce a pure sodium fluorohectorite sample (A more thorough description of the process is found in reference [4]). The clay is at ambient conditions in the hydrated 1WL state, and when clay in this state was investigated there was no need for further preparation before insertion. To get the clay into the 0WL hydration state it was placed in a furnace, holding a temperature of 150°C, for over three hours. The powder samples were inserted into the sample holder by screwing the two copper parts apart and placing it on the exiting kapton window before screwing them together again. The CO_2 used in this experiment had a purity of 99.7%. For this quality no specifications were available on the impurities in the remaining 0.3% of the gas. In the scans whith samples containing clay and CO_2, the samplevolume was flushed prior to exposure. This

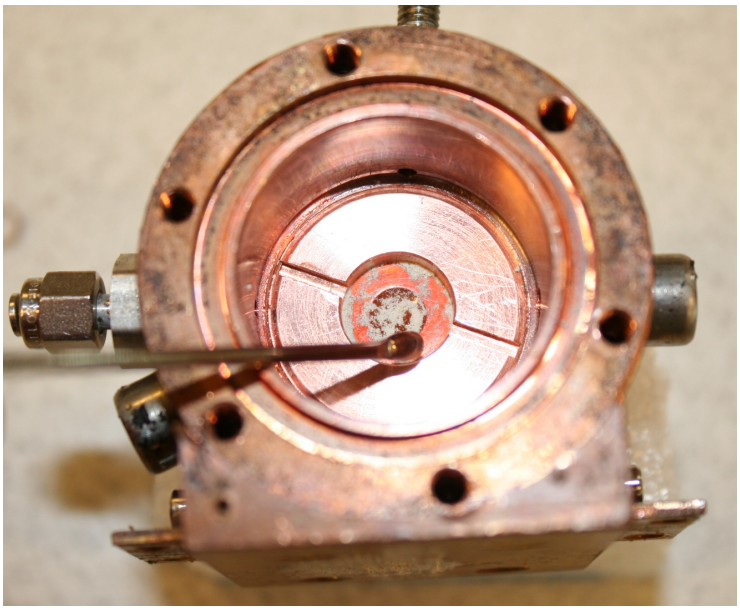

Figure 2.5: The powder samples were inserted by screwing the sample holder apart, and then placing them on the exiting kapton window.

was done by setting a pressure on the regulator valve and then slowly opening the plugged gas connection channel. A constant flow of CO_2 was then passed through the sampleholder for over one minute. In experiments with heated NaFh, efforts were made to minimize the time from insertion of the clay to the flushing of the cell, since the clay quite fast intercalates water vapor if exposed to humid air.

Imaging

Because of the little prior knowledge and what to expect from the experiment, the initial idea was to test the clay at different temperatures and CO_2 pressure. Since Fripiat et. al [5] had reported intercalation of CO_2 in smectites at low temperatures ($\sim -70^\circ$ C) and at atmospheric pressure, this was one of the conditions we would try to reproduce. However, as we could vary both the pressure, P, and temperature, T, we could take WAXS images over a wide range of temperatures, pressures and also at different hydration states of the clay. This resulted in over 60 scans of the NaFh-samples. The acquisition time differed between 30 to 120 seconds depending on the X-ray absorption of the sample.

2.2.2 Experiment at NTNU

Samples and preparation

The clay used in this experiment was the same type NaFh as used in the experiment at MAXII. This was done deliberately so that comparisons between the data from the two experiments could be made. The clay was heated for over 1 day. The CO_2 used in this experiment had a purity of 99.7%, but this was later changed to a CO_2 with a purity of 99.999%. The measurements done with nitrogen, was done with nitrogen with a purity of 99.6%.

Imaging

The time between the two experimental series gave us the opportunity to analyze the data from MAX-lab before the startup of the experiments at NTNU. This allowed a more systematic approach. Because of the almost constant access to the NanoStar, we now also had more time for performing each measurement. To get a high intensity to a good signal to noise ratio, the acquisition time had to be set to 1 hour. With this setting one unfortunately loses some of the dynamics in a intercalation processes. For these reasons it was also decided not to do experiments with liquid CO_2. Because of the higher density, liquids tend to absorb more X-rays than gas, hence reducing the intensity of the scattering and producing a poorer signal to noise ratio. Since the cooling process demanded some time and that low temperatures accumulates more frost on the kapton windows, it was decided not to go below -20°C. In all, over 600 scans were taken of the NaFh-samples.

Chapter 3

Data analysis and discussion

3.1 Data acquisition and processing

The following sections contains the procedure of transforming the frames obtained by the detectors, into the one-dimensional diffraction patterns used for the analysis.

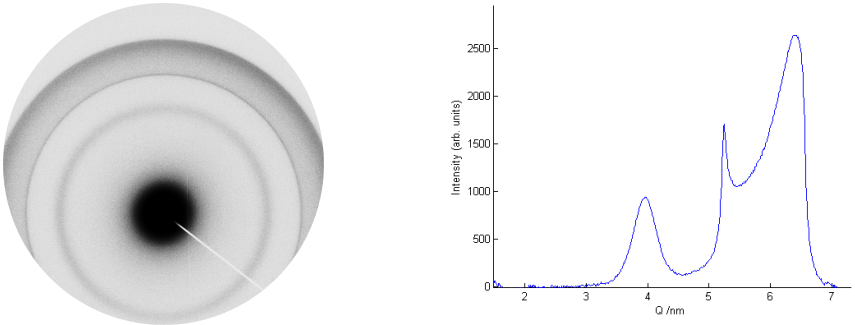

Figure 3.1: A frame (left) from a measurement carried out at MAX-lab and the one-dimensional diffraction pattern (right) from the same frame used for the analysis.

Frames

The data obtained by the detector are stored as pixel frames with binary raw data as well as information on spatial- and time coordinates in the frame header. For the MAX-lab data the header also includes the beam intensity at the time of exposure, since at synchrotrons the intensity varies during the time the beam is operational.

Fit2D

The Fit2D software was used for determining the detector-to-sample distance, finding the beam center and also integrating the frames. The radial integration of the pixel frames was done with respect to conic line segments, where one chooses the amount of averaging by setting the number of bins (resolution) in the output ASCII file. The size of the detector surface and size of the horizontal and vertical pixels is hence important parameters in this decision. The resulting one-dimensional diffraction plots show the intensity as a function of the scattering vector Q. Even though the data from the NanoStar also could be done by the SAXS software, the Fit2D was preferred because it is compatible with both types (MAXII and NanoStar) of data.

Matlab

For extracting the integrated plots, a Matlab script written by doctoral student Henrik Hemmen was used . In addition to running the Fit2D program and hence the integration, the script performed background subtraction, normalization on the integrated plots and made adjustments for the differences in intensities and counting times for the different scans. The individual parts will be described in the following subsections.

Calibration

To establish a correct position of the center of the beam and a correct sample to detector distance a calibration scan was performed. The calibration of beam center position and sample to detector distance was performed with a silver behenate powder sample which is known to have well characterized and well defined Bragg peaks [35]. When the diffraction rings are recognized, their positions are evaluated against tabulated values to produce a correct sample to detector distance and beam center. A correct beam position and sample to detector distance is crucial for the integration because they are directly related to the Bragg scattering angle θ.

Background subtraction

Background scattering decays with increasing angle and the small-angel scattering of monodisperse platelets are known to follow a power law [36]. Background was therefore fitted to a function of the form $a \cdot Q^b + c$. The intervals used for the basis of the fit were a region at lower Q than the kapton peak and a region at higher Q than the 0WL-peak. These regions are assumed to contain unessential scattering contributions for this study, i.e. only the background that we wish to subtract. Figure 3.3 shows the fitting of the background to the plot, and the resulting diffraction pattern after the fit has been subtracted for a chosen diffraction pattern. Because of background variations for the different exposures, an individual power law was fitted to each diffraction pattern.

Normalization

To try to make up for some of the difference caused by changes in beam intensity and absorption, the plots were normalized on a point in the curve that is not expected to be affected by changes in temperature and pressure. The peak due to the scattering from the kapton windows is not expected to vary and was therefore chosen for this purpose. The normalization was done by finding the intensity maximum value of the peak in a small region around this Q-value, and dividing the plots on this value. Although not that important when treating single diffraction patterns, when comparing two or more, normalization is very practical. If there are considerable difference in background noise, the diffraction patterns will often not coincide well even after normalization.

Peak position determination

When data allowed, the peak positions were determined by fitting pseudo-Voigt profiles (eq 1.23) to the data (see figure 3.2) and extracting the parameters from the fits. However, since this was not always an option for highly deformed peaks, some peak positions was just determined by finding the Q-position corresponding to the maximum intensity in the proximity of the peak. This of course given that the intensity at the peak maximum was above a certain noise-level. For the last method the accuracy of the peak position is naturally strongly limited by the resolution. The corresponding value of the d_{001}-spacing to the position of the peak is given by equation 1.14.

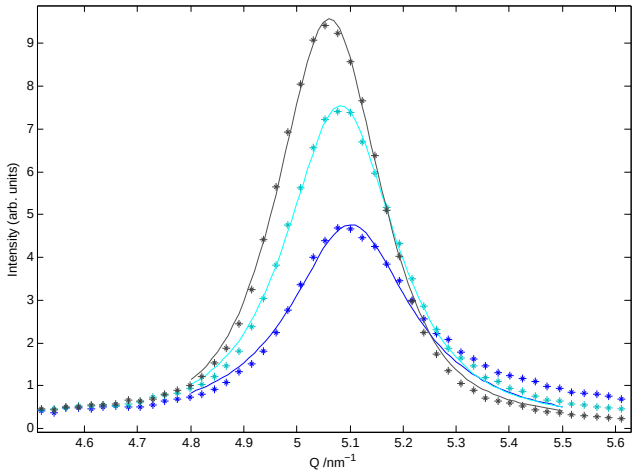

Figure 3.2: When it was possible, the data, 'dots', was fitted to a pseudo-Voigt profile, 'line'. This allowed for quite accurate determination of the peak position, by extracting the parameters from the fit, and hence the d_{001}-spacing.

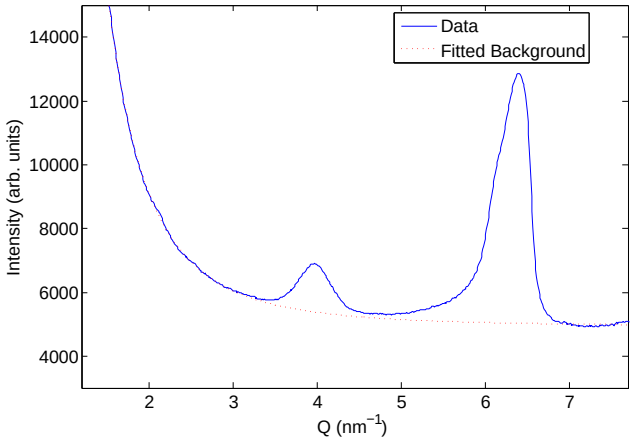

a) background fit

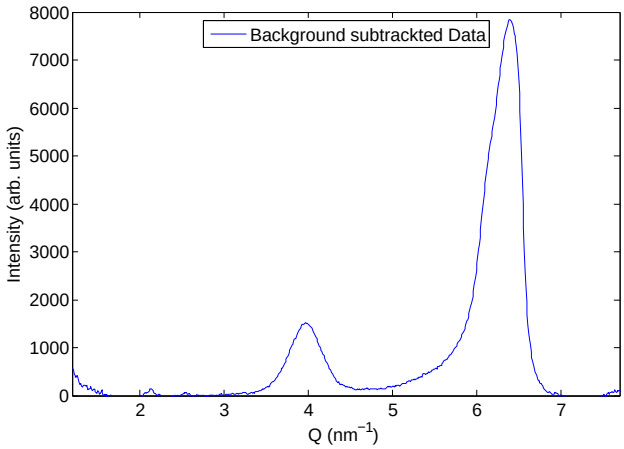

b) background subtracted

Figure 3.3: After a frame is integrated the background is fitted to a power law (a) evaluated on intervals not affected by the Bragg diffraction from the clay sample or kapton window. The fitted background is then subtracted from the data (b) and thus removing the unwanted noise.

3.2 Data analysis and discussion

In this section the results from the 'CO_2 intercalation experiment' conducted at MAX-lab in Sweden and at NTNU in Trondheim will be presented. During the time of the experiment and as it progressed, question usually arise from the data at hand. The next natural step in the process was then often to think of and carry out new measurements that could provide answers to these questions. I therefore find it convenient to present the different sub experiments in a more or less chronological order after when they were performed. In each part I will discuss the results as they stand alone and/or compare them to the previous results, while in the end of this section you will find a more comprehensive discussion of the the results of the experiment as a whole.

3.2.1 MAX-lab data

1WL and CO_2

The NaFh is in the 1WL hydration state at ambient conditions. A natural starting point for the experiment was therefore to look at the clay in this hydration state when exposed to CO_2.

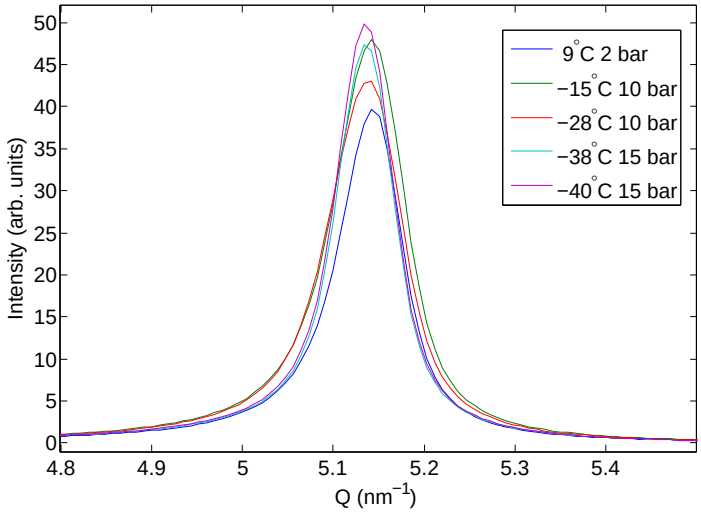

Figure 3.4: Diffraction patterns of the sample in the 1WL hydration state exposed to CO_2 at different temperatures and pressures. Small shifts in the peak position, relating to changes in the d-spacing, can be observed. However these shift are estimated to be small compared to the changes experienced of NaFh in the 1WL state. Pressure is given as pressure over atmospheric pressure.

Diffraction patterns of the NaFh powder in the 1WL hydration state exposed to CO_2 at different temperatures and pressures are shown in figure 3.4. The 1WL

peak is pronounced for all the patterns and except for difference in width[1], the peaks seem to represent the same stacking geometry; all the clay particles contain the same d_{001}-spacing at the different conditions. Examining the difference between the patterns there might look like there are small shifts in the peak positions which would indicate small changes in the d-spacing. However when fitting Pseudo-Voigt profiles to the peaks, these shift are estimated to be less than 0.02 Å. As reported by Hemmen et. al [1], there can be shifts of ∼0.3 Å also within the hydration states when changing the pressure, temperature and humidity conditions. Hence it would be bold to attribute these shifts to anything other than expected variations. There are no significant difference between the plots that would indicate any intercalation of CO_2 or any interaction that alters the structure of the clay. It is not known if the CO_2 molecule can penetrate the interlayer space without evicting water molecules or forming a joint 'second' layer, hence not changing the d-spacing. Since this can not be measured with diffraction, this remains as speculations. It is more likely that when in hydrated states, the NaFh is unable to intercalate CO_2 in the temperature and pressure regions of investigation. The density of water vapor when intercalated is almost that of liquid water, and as the power of the interlayer sink is very high compared to concentration of water in vapor form [37], the 1WL-hydration state could be considered a more energetically favorable state than an eventual pure state of intercalated CO_2. Another point is that the water molecules are polar while the CO_2 molecules have a zero net dipole moment which means that they likely may not mix. This can prevent the water from leaving the interlayer space. If one look at the phase diagram of CO_2 (figure 1.6) one can see that the measurements shown in figure 3.4 were obtained in presence of liquid and gaseous CO_2. Because of the minor differences between the plots, the physical state of CO_2 does not seem to have any effect on the interaction between the CO_2 and the clay sample in the 1WL-state.

Varying pressure

The first interesting result was observed in the measurements performed with the heated NaFh clay (starting in a pure 0WL hydration state). This is seen in figure 3.5 which show the recorded diffraction patterns taken when the temperature was held constant at -20°C and the pressure of the CO_2 was increased stepwise with a time of approximately 5 minutes between each scan. All scans are taken within the gaseous phase of CO_2 (see CO_2 phase diagram, figure 1.6). The peak positioned at $Q \sim 6.4\,\mathrm{nm}^{-1}$ is due to the Bragg diffraction of the d_{001}-spacing for the clay particles in the 0WL hydration state. One notices that the 0WL peak has a asymmetric shape to begin with (measurement done at 1 bar), with a shoulder on the left side. The peak also seem to decay differently on the two sides of the peak maximum. This peculiarity is mentioned later in a special section, but is not an effect of CO_2. If directing the attention to what seems to be the effect of increasing the pressure, the plots shows two clear features: one is the

[1]Peak width is not a subject for this study and will not be treated further.

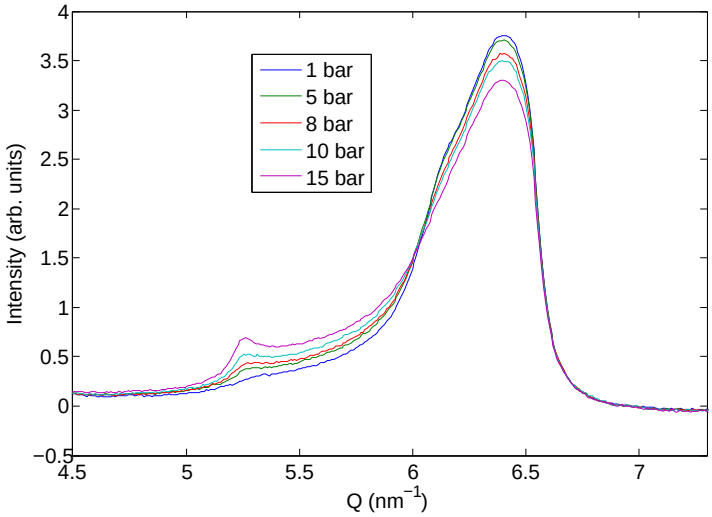

Figure 3.5: Diffraction patterns of NaFh exposed to CO_2 at -20°C taken at different pressures. The peak appearing at $Q \sim 5.25\,\mathrm{nm}^{-1}$ increase with increasing pressure indicates that some of the clay particles have intercalated a substance, leading to a change in d-spacing. The pressure is given as pressure over atmospheric pressure.

decrease of intensity of the 0WL-peak when increasing the pressure, the other is the opposite behavior of the peak appearing at $Q \sim 5.25\,\mathrm{nm}^{-1}$. This indicates that a proportion of the clay particles in the scattering volume have intercalated a guest substance, as described in section 1.1.2, causing an abrupt change in the d_{001}-spacing of approximately 2 Å. As the peak grows, an asymmetry reveals itself also for this peak. The asymmetry, partly due to the already existing asymmetry of the 0WL-peak, is seen by the peak intensity increases, and also by a broad distribution on the right side of the peak. The intensity of this shoulder increases with increasing pressure. This broad distribution reveals a possible coexistence between the 0WL and the intercalation state, in which case the Hendricks-Teller [29] formalism applies.

Varying temperature

The previous measurements showed evidence of a intercalation process with gaseous CO_2, and the amount of clay particles which were intercalated seemed to increase when increasing the pressure. The set of diffraction patterns, seen in figure 3.6, corresponds to the measurements that were taken with the NaFh exposed to CO_2 at 15 bar (held constant) when the temperature was progressively decreased between consecutive scans. The time between the scans were approximately 5 minutes.

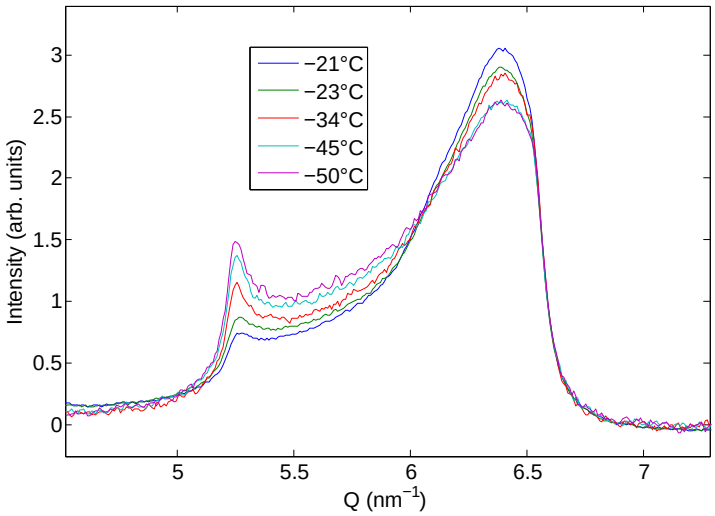

Figure 3.6: Diffraction patterns of NaFh and CO_2 at 15 bar at different temperature. The change of intensity of the two peaks indicates that more clay particles in the sample volume intercalate when the temperature is decreased.

It is clear that some intercalation has already occurred on the first scan, at 15 bar and -21°C, with a slight bump apparent at $Q \sim 5.25\,\mathrm{nm}^{-1}$ in the diffraction pattern. The previous measurements had shown that there was some intercalation at pressures also lower than 15 bar (see figure 3.5). So when the cooling required a certain time, some intercalation at this stage is also to be expected based on that measurement. Compared to the previous case we now see that the peak due to intercalation is much more pronounced, but the ratio between the two peaks reveals that the largest fraction of the clay particles still contain the 0WL-state basal spacing. Figure 3.6 suggests that temperature have a similar effect on the intercalation peak as the previous measurements where the pressure was varied. The 0WL peak is decreasing, the left side of the intercalated peak is starting to show clear Bragg peak characteristics as it grows, while the broad distribution in between the two peaks further implies the coexistence of various mixed-intercalation states. All these characteristics seem to strengthen as the temperature is decreased. It is clear that also the noise increases when the temperature is lowered, which unfortunately makes the basis for comparison of the patterns worse. This is probably due to absorption of X-rays caused by the CO_2, which one should expect to increase when crossing the transition into the liquid phase. At 15 bar the transition to liquid occurs at ∼-25°C (see figure 1.6). Frost on the kapton windows was also observed, which would also contribute to more absorption of X-rays, and hence more noise at lower temperatures.

Time dependence

In the previous measurements it appeared that decreasing the temperature or increasing the pressure of the CO_2, caused increasing intercalation. The effect seen in both cases could however just as well be attributed another important factor: time. Although they might show the characteristics of the transition between states, they reveal nothing of the time dependence of the process. In the previous measurements the sample had not been held at the same condition for any long time, and actually when assigning the degree of intercalation to changes in temperature and pressure, one is assuming a fast saturation at the different conditions. This is not given, and before exploring the temperature and pressure effects further, it was clear that to better understand the dynamics of the intercalation process one should look closer at the time dependence.

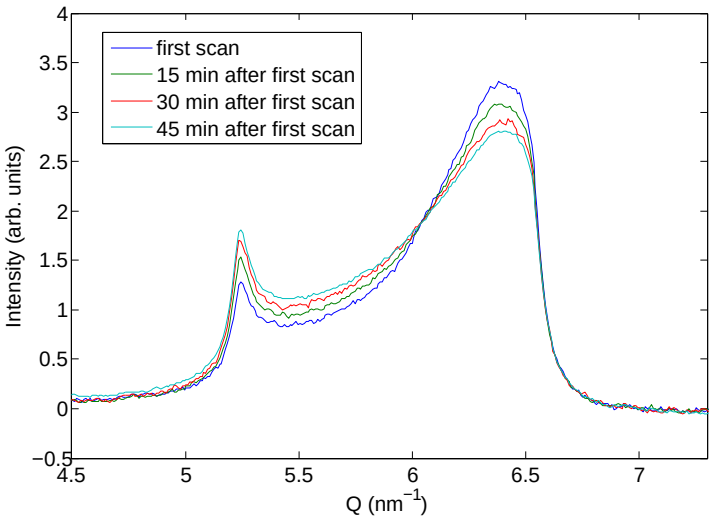

Figure 3.7: Diffraction patterns of NaFh and CO_2 at -40°C and 15 bar. Pressure is given as pressure over atmospheric pressure.

Figure 3.7 shows the evolution of the 001-Bragg peak when both the temperature and the pressure are held constant, -40°C and 15 bar (over atmospheric pressure) respectively. The measurement were done with the exact same sample as that displayed in figure 3.5, but after cooling it further to reach -40°C (liquid phase) at the end of the last scan in that series. Being held at these condition for a given time is therefore the reason why intercalation already had occurred. If one look at the time evolution it is obvious that time is an important factor as the measurements show the same features as seen in figures 3.5 and 3.6, but now as the function of time. The rate however seem to be very slow, as only there appear to be a relatively small increase in the intercalation during the 45 minutes time period.

Dynamics

The previous measurements showed proof of dynamics that deserved further investigated. To really understand the effects of temperature and pressure it became obvious that a longer waiting period was needed when the condition were changed. The results of this approach is shown in figure 3.8 were the time evolution at six ((a)-(f)) different temperature and pressure conditions are seen. Each figure contains a diffraction pattern of a reference scan, that was taken directly after the conditions were set, and a diffraction pattern taken thirty minutes after this.

While there are small, if any, visible differences between the diffraction patterns in figure 3.8 for each of patterns in (a), (b) and (c), there are visible changes for (e) and (f) at 10 bar -20°C and 15 bar -20°C, respectively, and to a certain degree also for (d) at 5 bar and -20°C. The changes are seen by the difference in intensity around the area of the peak due to intercalation, more than the difference in intensity of the 0WL-peak. This indicates that the intercalation observed has a certain time dependence as discussed above, but also that the pressure and temperature conditions are determining the rate of the process. It is also clear that the temperature and pressure do not control the rate independently, since there are not seen any big difference in (b), 15 bar and 20°C, or (c), 1 bar and -20°C. The measurements do not exclude that intercalation also occurs at higher temperature and lowered pressure, but certainly not within the time frame of thirty minutes. The time evolution can in all cases be considered slow in the way that it is better expressed in hours rather than minutes.

3.2.2 Short discussion of the MAX-lab data

It might be tempting at this point to firmly claim that the results indicate intercalation of CO_2, and I myself will argue this later. However as there are some uncertainties regarding the process I will until further keep addressing it as the intercalation of a guest substance. Fripat et al. [5] reported the intercalation of CO_2 with the use of X-ray diffraction and by IR absorption into homoionic smectites in 1973. In this report they argue that a reflection cannot be assigned to the adsorption of water impurity, if it is not maintained after the sample is rewarmed. Based on the experience that the conditions needed for removing intercalated water vapor from the NaFh clay was to heat it for hours at high temperatures (>100°C), it is easy to draw this conclusion. What our results showed (fig. 3.9) was that when rewarming the sample from conditions where the peak from the intercalated state was visible, one sees a significant drop in intensity of the peak. Which if standing by Fripiats argument would prove that CO_2 is the intercalated substance observed. However his argument falls a bit short in our case since certain conditions of the relative humidity have also been shown to cause water to leave the interlamellar space [1]. Hence one can not rule out the possibility of water intercalation.

The peak that is observed is not representing a pure and stable state, and only a fraction of the clay particles in the sample volume have been subjected to intercalation and changed d-spacing. The position of the peak is therefore at this point, not a good method for determining the substance that is intercalated. As the amount of clay particles in an intercalated state will increase with time, the d-spacing might change in a similar fashion like experienced with water intercalation [1]. As an example of this, some articles state the value d_{001}= 12.2 Å for the 1WL basal spacing of NaFh [2]. This value is however, as stated, the mean basal d-spacing. As seen in figure 3.10, which is the scan of a sample that was not heated for the acquired amount of time to get a pure 0WL peak, the 1WL-peak is positioned at a Q-value corresponding to a d_{001}-spacing of $\sim$ 11.9 Å. This is 0.3 Å less than the mean. Since the peak observed is not from a pure intercalation state, there might as well be changes of the same magnitude in the d-spacing during the transition into a pure state also in this case.

0WL peak

A feature of the diffraction patterns which was just mention briefly above, is the shoulder that can be seen on the 0WL peak. The peak is also asymmetric in the way that it has a difference in decay, uneven distribution, on each side of the peak maximum. A scan was taken with the heated sample without flushing the cell with CO_2, and this also showed a diffraction pattern of the same shape as the 0WL-peak of samples exposed to CO_2. The shoulder is therefor not due to the presence of CO_2. The uneven distribution could therefore indicate a partially ordered 0WL state. If this partially ordering comes from the presence of a small amount of residual water after heating, it might be explained by the existence of Hendricks-Teller mixed intercalation state [4, 29], a coexistence of the 0WL and 1WL hydration state.

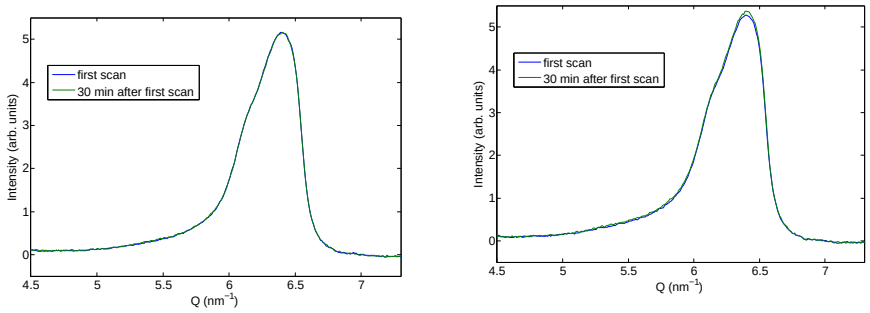

(a) 1 bar 20°C

(b)15 bar 20°C

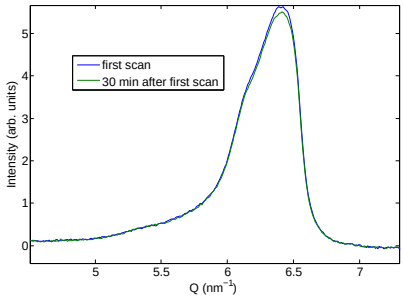

(c) 1 bar -20°C

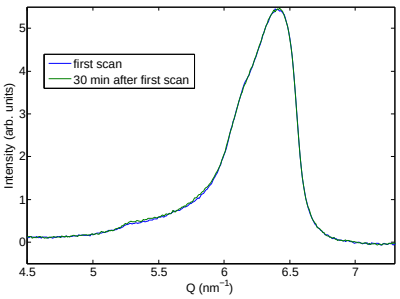

(d)5 bar -20°C

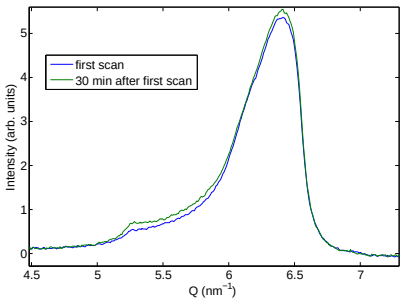

(e) 10 bar -20°C

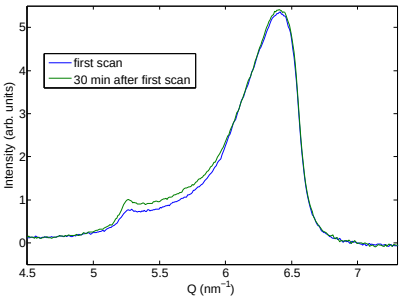

(f)15 bar -20°C

Figure 3.8: To determine the time dependence of the intercalation process, two measurements were taken at each conditions for temperature and pressure. The first one is taken directly after the conditions are set while the second one is taken after thirty minutes holding time. For (a)-(d) the differences between the diffraction patterns are indistinguishable. For (e) and (f) there are however small, but visible changes between the two measurements.

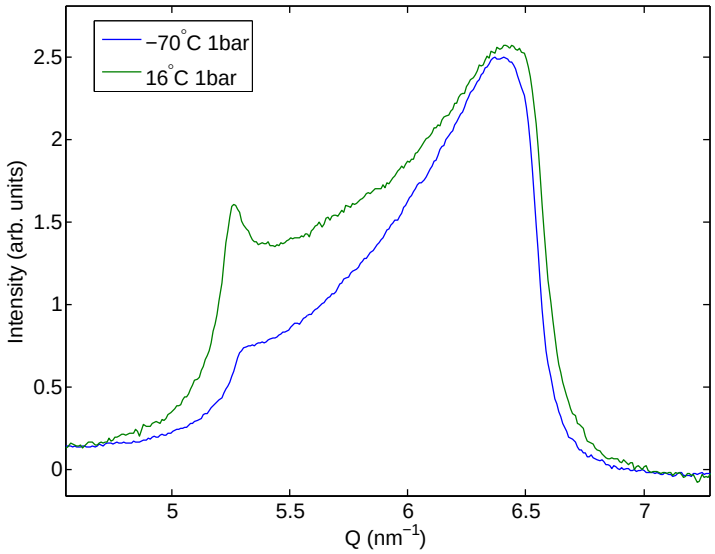

Figure 3.9: Diffraction patterns showing the drop in intensity of the intercalation-peak when the sample was warmed from -70°C to 16°C. Pressure is given as pressure over atmospheric pressure.

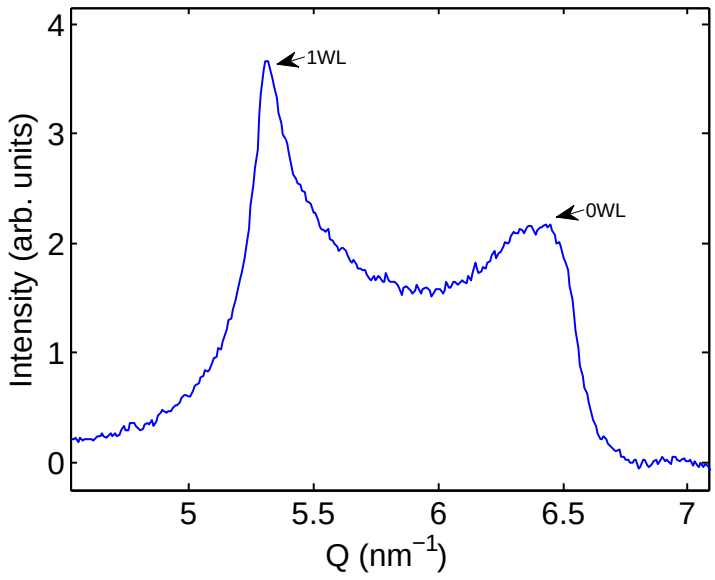

Figure 3.10: The diffraction pattern of a not fully dehydrated NaFh sample where the Bragg peaks from both the 0WL and 1WL basal d-spacing is evident.

3.2.3 NTNU data

Establishing that the intercalation process under investigation was very slow, implied that getting a clear peak would acquire waiting quite some time. A clear peak would give a more accurate value for the d_{001} spacing and possibly help identifying the intercalated substance. The obvious next step was therefore to keep the clay under the same conditions where the intercalation process had been observed at MAX-lab and keep it there without interfering, taking consecutive scans along the way. With the intensity drop due to the absorption of X-rays in liquid CO_2 and the lower X-ray intensity provided by the Nanostar than at MAXII, it was decided to focus on the gaseous phase of CO_2 to ensure good statistics. The MAX-lab data had also shown that intercalation occurred in this phase.

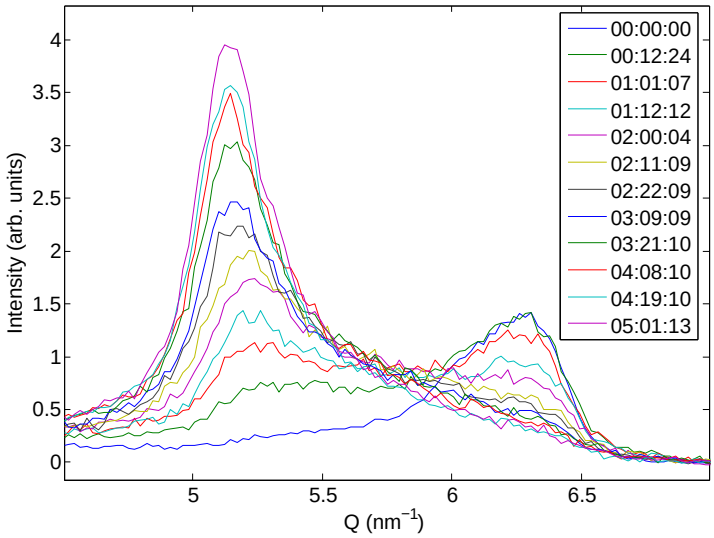

Figure 3.11: The slow intercalation process is seen as the 0WL-peak became weaker with time, while the peak appearing at $Q \sim 5.25\,\mathrm{nm}^{-1}$ was getting stronger. Experiment at -20°C and 15 bar CO_2. The plot legend show the lapsed time after the first scan in days, hours and minutes (DD:HH:MM).

The time evolution of the 001-peak at the conditions -20°C and 15 bar (except the first diffraction pattern, a reference scan which is taken at room temperature) during the transition from the 0WL-state to the intercalated state is shown in figure 3.11. As can be seen by the plot legend the measurement lasted for over five days. Like observed and discussed in the previous sections we also here see that there is intercalation of a substance indicated at first by changes in the shape of the 0WL Bragg peak as it gradually becomes more asymmetric and a new peak appears at $Q \sim 5.25\,\mathrm{nm}^{-1}$. As the time passes an intensity distribution develops in-between the positions for the two peaks, until the 0WL-peak is in the end more or less disappears beeing replaced by the peak

due to intercalation. The decay on the right side of that peak suggests that it does not represent a pure state and that one could expect a further growth of the peak if kept longer at these conditions. However it is clear that the main proportion of the clay particles in the sample volume at this time are in an intercalated state. The transition bares resemblance to the transition for NaFh from the 1WL to 2WL-hydration state, reported by Løvoll et al. [4]. One notices that there is great difference in intensity and area of the two peaks, which is mostly due to the layer structure factor of the NaFh (eq.1.8) and the Lorentz-polarization factor (eq. 1.17). The intercalation state is positioned at a Q-value corresponding to the basal spacing $d_{001} \sim 12.2$ Å. This means that the unit cell has expanded with approximately 2.2 Å in the 001-direction. One also see that before reaching this state there are changes in the d-spacing, which is indicated by the gradual shift of the peak maximum. If the peak is not representing a pure state as proposed, an even bigger d-spacing value can be expected. This expansion is close to that of the basal spacing in the 1WL hydration state [2].

Water vs. CO_2 Intercalation

Because the position of the peak is close to that of the NaFh in the 1WL hydration state, it is natural to ask the question: could the peak be due to water and not CO_2 intercalation? And if so; how did the water get into the cell? The cell was flushed with CO_2 prior to exposure to ensure that no air was in the sample volume. Aylmore [38] criticized Fripat et al. for using a relatively mild outgassing procedure, and that residual water molecules could explain the intercalation that they observed in their experiments. The same criticism could be directed to the flushing procedure used in this experiment, since no measurements could be performed to verify how successful this method of removing the air really was. Residual water molecules could originate from water vapor in the cavities of the sample holder and also from a water film on the copper surfaces inside the sample holder. It has previously been shown that the d-spacing can be expressed as a function of relative humidity, and that changes in the relative humidity induce changes in the d-spacing [1]. The relative humidity (RH) is defined as the ratio between the partial pressure and the saturation vapor pressure and is dependent on both temperature and pressure [39]. The RH will increase both when increasing the pressure and when decreasing the temperature. Changing these two parameters could therefore affect the intercalation process if humid air is present. It is possible to assume that the clay was packed in the sample holder in such a way that traces of water vapor surrounding the clay in the sample cell was transferred into the clay and to the part which was subjected to the incident X-ray beam. As humidity transport is rather slow in this sample (days/cm) [1], it will take some time before the intercalation front reaches the center and a pure hydration state is seen on the diffraction patterns. In this particular experiment, if water molecules are to intercalate in the first place, there has to be enough water inside the sample holder to fill up the host layers. In an attempt to verify/disprove this, a sample was prepared without no prior flushing of CO2. The gas connection was instead plugged after the clay

was inserted so that the amount of residual water inside the sample holder would be constant. With this setup it was not possible to pressurize the sample holder, and the clay was only kept under ambient pressure. On the other hand; because the sample holder was not subjected to any flushing, the amount of water inside should be greater compared to the flushed sample holder. The temperature was set to the same as that of the previous experiment, -20°C, after a reference scan at room temperature was taken. Note that at this temperature one should also expect that the water vapor would freeze when in contact with the surrounding copper, so not all the amount of water inside was able to intercalate the clay.

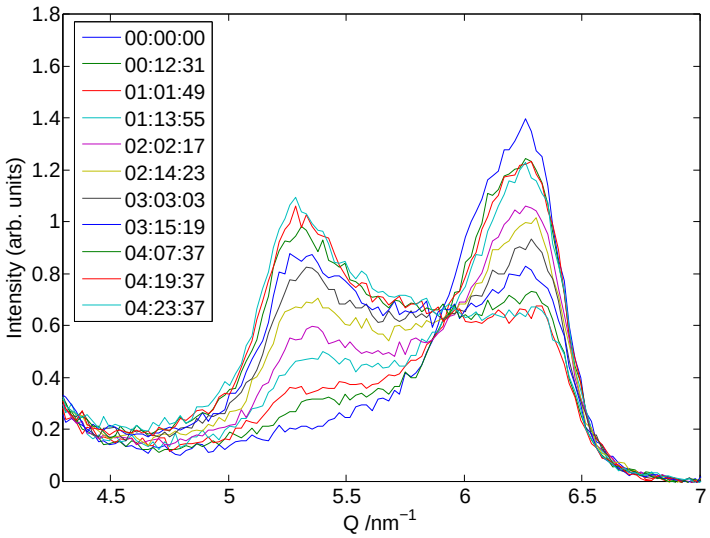

Figure 3.12: Water intercalation from the residual water inside the sample holder. The intercalation is slow compared to the previous measurements figure, with both the 0WL and 1WL peak present after 5 days. The plot legend show the lapsed time after the first scan in days, hours and minutes (DD:HH:MM).

Figure 3.12 shows a selection of the one-dimensional diffraction pattern measured with the NaFh when in presence of the air confined by the sample holder volume. The time evolution reveals that there is intercalation of water, as the 0WL-peak is gradually decreasing and the 1WL-peak is inversely rising. Compared to the measurement with CO_2 (figure 3.11) the intercalation process observed here is much slower. While the diffraction spectra measured with the clay exposed to CO_2 had a clear intercalation peak after 5 days and no 0WL-peak (see figure 3.11), both the 0WL- and 1WL-state are evident after the same time had passed for this measurements. Having in mind the effect of the layer structure and Lorentz-polarization factors, a considerable proportion of the clay particles within the sample volume still contain a 0WL d-spacing. One can expect that a pure 1WL would eventually be reached, if given the enough time, since the process does not seem to have reached saturation at the end

of the measurements. This leads to the conclusion that the water confined by the sample holder volume is enough to cause a transition from the 0WL to the 1WL hydration state. However the rate at which the residual water molecules in the sample holder intercalates questions the possibility that this is the same transition as observed in the previous measurements. When comparing rates, one should have in mind the effect packing of the clay sample has on the process. More clay and a closer packed sample would lead to slower intercalation than less clay and a loosely packed sample. For this experiment the packing of the samples was considered sufficiently equal so that the difference (days) between the two measurements could not be from packing effects. This leads to the conclusion that there needs to be an additional factor if residual water in the sample holder is the cause of the intercalation observed in the previous measurements.

Flushing with Nitrogen

The previous set of measurements showed that the water inside the sample holder intercalated, but at a rate much slower compared to the case with CO_2. Since the flushing of the cell with CO_2 would reduce the amount of water in the cell, the higher applied pressure could be the reason for the still higher rate of intercalation observed with the clay exposed to CO_2. This of course given that water was in fact the intercalated substance. To find an answer to this, nitrogen gas was used instead of CO_2, since this could provide approximately the same conditions for pressure and the flushing would be the same. Nitrogen penetration into the interlamellar space is reported for montmorillonite[2] to depend on the packing and influence of the interlayer cation, but the penetration does not progress to allow significant expansion of the host layer [38]. A notable change in d-spacing or transition caused by intercalation of nitrogen is therefore not to be expected. In addition to providing the same pressure, this measurements would also give some answer on how effective the flushing method is.

In the diffraction patterns in figure 3.13 measured with NaFh and nitrogen at -20°C and 13 bar[3] one can hardly see any signs of intercalation. After two days the main proportion of clay particles are in the 0WL-state. When comparing the last couple of diffraction patterns in the sequence with the first one, one might notice a slight bump in the spectra appearing in the region where both the 1WL-peak and the peak in interest was observed. Comparing the intensity increase of this bump with respect to the lapsed time, with that of the intensity increase in the measurements when the NaFh was exposed to CO_2 (figure 3.11) or even with the NaFh exposed to air, this increase can be considered relatively small. The small increase is also not much different from the noise level, which further implies its insignificance.

Based on the previous test/experiments we can with confidence say that the

[2] Like NaFh, montmorillonite is 2:1 smectic clay.

[3] Ideally this should have been put at 15 bar, but unfortunately this was not possible with the nitrogen regulator.

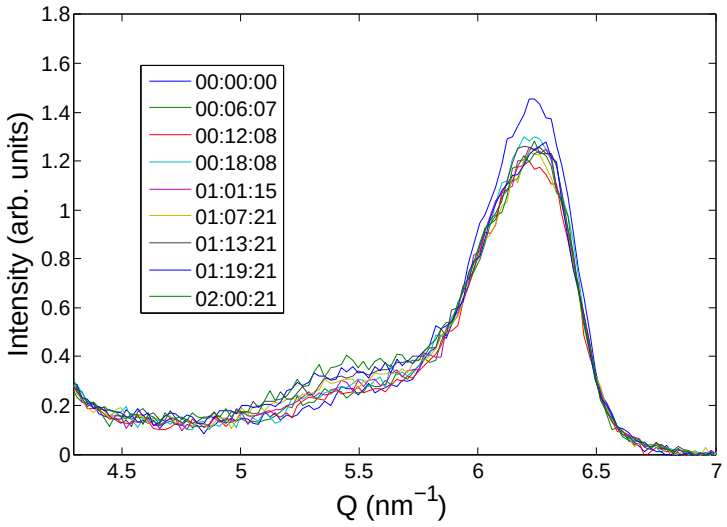

Figure 3.13: Diffraction patterns of the measurements of NaFh when exposed to nitrogen gas. The plot legend show the lapsed time after the first scan in days, hours and minutes (DD:HH:MM).

peak observed in the samples with CO_2 does not come from residual water inside the sample holder. Based on this conclusion, also the flushing method could be considered satisfactory.

Pure CO_2

During the previous discussion, it was argued that the flushing procedure would remove enough of the residual water inside the sample holder to prevent it from being the intercalated substance leading to the peak observed in figures 3.5-3.8 and 3.11. The only other explanation for how water could get into the sample holder, is then through the CO_2 gas, which contains impurities. As mentioned in section 2.2.1, the CO_2 used had a impurity content of 0.3%. This could lead to intercalation if this percentage mainly consisted of water. For the next experiment, CO_2 with a 99.999% purity was used instead. Of this gas only 2 ppm is subscribed to H_2O. With such a low percentage of water, the pressurized gas could not provide enough water to cause a transition into the 1WL-hydration state.

From the results shown in figure 3.14 it is clear that we have intercalation of CO_2. With a very low content of residual water in the sample holder, secured through the flushing method, and no water vapor in the CO_2 gas, secured through using a pure gas, leaves the incorporation of the CO_2 molecule in the interlamellar space as the only other possible subject for causing the d-spacing to increase. This time it was also made sure that the intercalation proceeded until

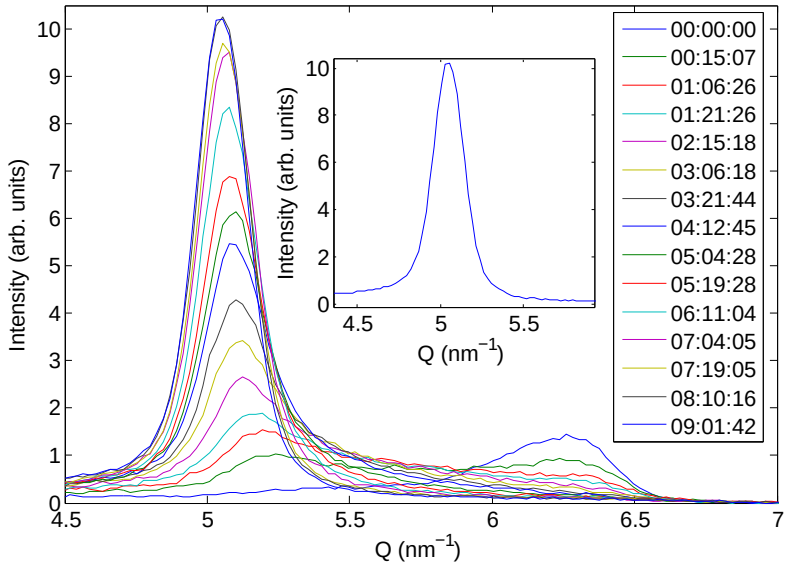

Figure 3.14: Diffraction patterns of the measurements of NaFh exposed to CO_2 that had a low impurity content. The plot legend show the lapsed time after the first scan in days, hours and minutes (DD:HH:MM). The inset shows the diffraction pattern from the last scan of the measurements. The symmetry of the peak reveals that it represents a pure intercalation state. Temperature: -20°C, CO_2 pressure: 15 bar.

a pure intercalation-state was reached, by keeping the measurements going for over 9 days. The high degree of symmetry of the peak at the last measurement verifies that this is in fact the case.

The time evolution of the d_{001}-spacing of the same measurement are shown in figure 3.15. The red dots mark the d-spacing based on the fit of pseudo-Voigt profiles, while the blue dots mark the d-spacing evaluated by the position of the peak maximum when that value of the intensity is twice that of the average in a small region ($5.5 < Q < 6.0$) between the peaks. It is clear that the last method is strongly limited by the Q-resolution. The plot shows that the d-spacing is following a gentle curvature, almost linear increase (~ 0.03 Å/day), after the main proportion of clay particles in the sample volume are in the intercalated state. From the time the peak was first well enough defined so that pseudo-Voigt fit could be made (approx. 90 hours) and until the end of the measurement, the d-spacing has shifted $\sim$0.15 Å. Including the calculations of d-spacing based on the peak maximum, the total change is estimated to be 0.4 Å. The resolution of the detector is however of 0.06 Å so the actual total change can be expected to be something in-between these two values. It is quite remarkable that, although very slow, the d-spacing does seem to reach saturation even after the sample

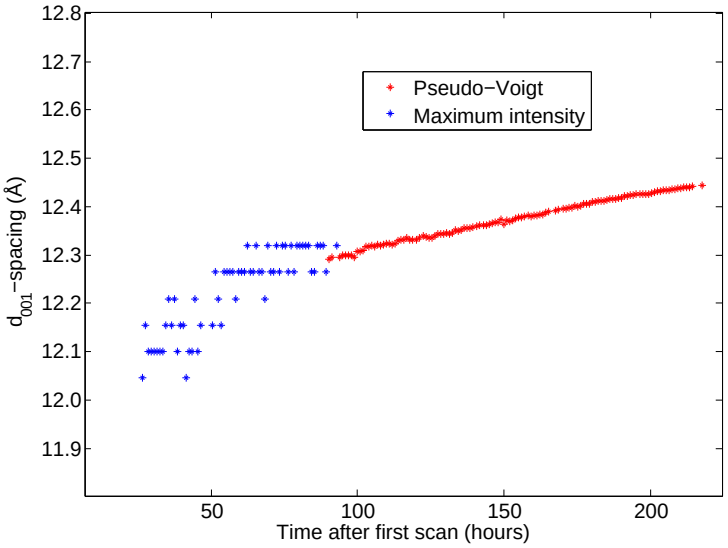

Figure 3.15: Time evolution of the d_{001}-spacing. The blue dots represent d_{001}-spacing values determined by the peak position that corresponds to the maximum intensity. The red dots represents the d_{001}-spacing values determined by the pseudo-Voigtian fit.

has been held at the same conditions for over 9 days. Basing calculations on the d-spacing evaluated by the fitted pseudo-Voigt profiles, the mean basal spacing is estimated to be 12.38 ± 0.04 Å. For comparison, in appendix A the mean basal d-spacing for NaFh in the 1WL-hydration state at -20°C is calculated to $12.36 \pm 3.96 \times 10^{-4}$ Å.

After approximately 220 hours the pressure of CO_2 was released, the gas connection opened and the temperature increased to 20°C. The silica gel inside the sample chamber was also removed so that vapor water would be present and eventually intercalate. Looking at figure 3.16 one can see that this resulted in an abrupt but very small change of d_{001}-spacing of $\sim$0.06 Å when plotting the d_{001}-spacing as a function of time. The corresponding diffraction patterns to this abrupt change, show no form for transition between states, but the shift of the peak can also bee seen there. Because of the long exposure time (1 hour) and hence bad temporal resolution, it is clear that some of the dynamics have been lost, and that the change might contain more information than what is seen here. However with the overall rate of intercalation beeing so slow, it is likely to believe that big changes will not occur. A mentionable feature is still the way the d-spacing seem to saturate back towards a higher value after the abrupt change has occurred. One could expect a shift of d-spacing also within hydration states when changing the condition, but it is not clear why this will cause an over shooting, explained by that the lamellar sheets first contracts 'fast' followed by them pulling apart slowly as they saturate. The curvature of

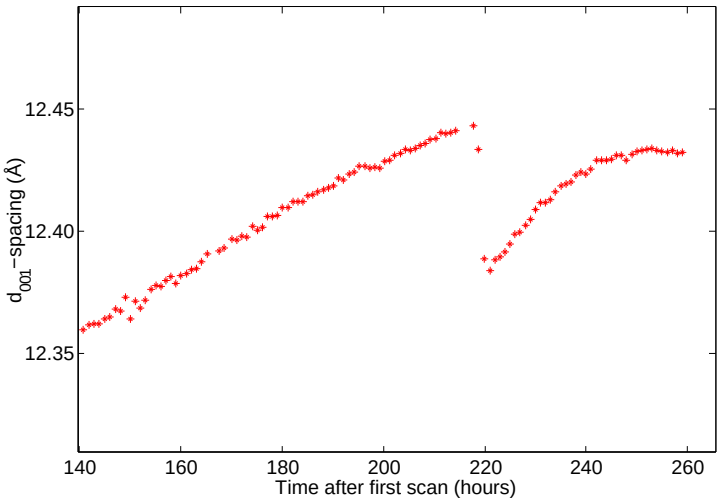

Figure 3.16: Time evolution of the d_{001}-spacing in the region where pseudo-Voigtian peak fit was performed. After approximately 200 hours the pressure was released, the gas connection opened and the temperature set to 20°C. This resulted in a abrupt, but very small change, followed by a slow gradual shift of the d-spacing.

the plot is also higher, hence a faster saturation, after the cell is opened than before. A transition where the CO_2 is diffusing out of the sample while the water is at the same time intercalating could explain this behavior, but the change is however so small that its significance should not be exaggerated or given too much attention.

Effect of pressure

After establishing the time dependence of the intercalation of CO_2 at a certain condition, it was again time to direct the attention back to the effect of pressure (seen in figures 3.5 and 3.8). This was done by doing the same type of measurement, but by setting a different CO_2 pressure. This would give a better picture of the relationship between the rate of the intercalation and the pressure. The results are shown in figure 3.17 and they were obtained at -20°C and 5 bar CO_2.

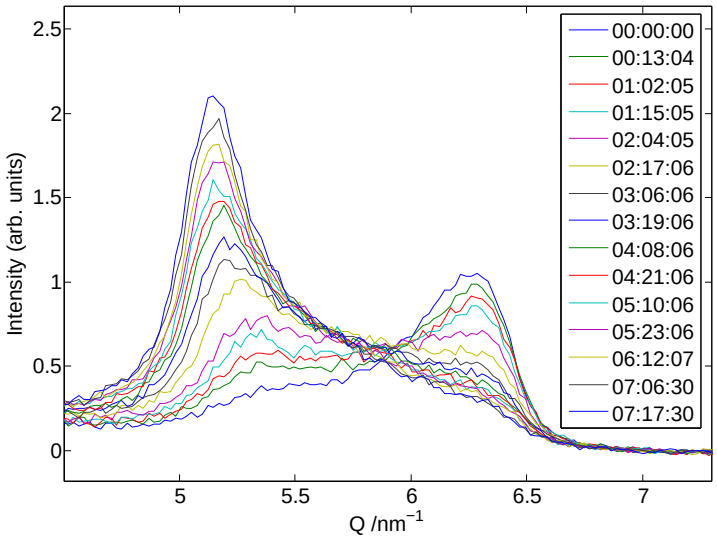

Figure 3.17: Diffraction patterns of the NaFh exposed to 5 bar of CO_2 at -20°C. The plot legends show the lapsed time after the first scan in days, hours and minutes (DD:HH:MM).

When comparing figures 3.14 and 3.17 the effect of pressure is obvious. When the pressure is set to 5 bar, it results in a intercalation rate much slower than at 15 bar. Still it is intercalating at conditions for temperature and pressure not far from ambient.

3.2.4 Discussion

The measurements I have performed show that CO_2 is able to intercalate in NaFh at conditions not too far from ambient. The proof is based on the fact that I have disproved the possibility of water intercalation (the only other possible subject), more than I have proved directly the presence of CO_2 in the interlayer. It has been found that the orientation of the water molecules in the single layer hydrate is in such a way that one of the OH bonds of the water molecule points in a direction almost perpendicular to the silicate layers[4] [40]. If assuming that the CO_2 molecules arrange with their long axis parallel to the silicate sheets, one can expect that there is a difference in the d_{001}-spacing when the two substances are intercalated in the clay. With the basal spacing of the clay with intercalated CO_2 beeing slightly smaller. The molecular dynamics simulations completed by Cygan et al. [12] on sodium montmorillonite computed a mean basal d-spacing of 12.23 Å for intercalated CO_2, which is in fact 0.1 Å smaller than the observed spacing of 12.35 Å for water. In the results I

[4]Actually two different sites for water molecules are observed. The one described here is the most abundant.

have presented the d-spacings from the pure CO_2 intercalation state is indistinguishable (<0.05 Å) from the 1WL hydration state (Appendix A). And it is clear that if this is close to the actual difference, the identification of CO_2 as the intercalated substance based only on the d-spacing itself would require more accurate measurements with much higher resolution. We already know that the d-spacing of NaFh during intercalation of water vapor, and also during the CO_2 intercalation reported here, experience shifts (∼0.3 Å) within the intercalated state. These shifts are even greater than the estimated difference between the d-spacings proposed by Cygan et al. Hence it is clear that even with high resolution measurements it would be difficult, if even possible, to distinguish H_2O or CO_2 intercalation based on d-spacing values alone. The requirement of a stable intercalation state is also difficult to achieve, as the basal spacing use very long time to stabilize within the accuracy of 0.1 Å, if it even stabilizes at all (cf. the increase of the d-spacing seen in figure 3.15, show no clear sign of having reached saturation after 9 days). The results presented by Wang et al. [6] of the CO_2 intercalation in 2:1 aluminosilicate phyrophyllite suggest that infrared spectroscopy is an alternative way of determining the intercalated substance.

If one accepts the claim of that what is reported here is CO_2 intercalation in clay, it is time to ask why the rate of the intercalation process depends on the pressure and temperature. A quantitative description of the clays swelling behavior is very challenging because of the complexity of the swelling clay system. The intercalation is however a result of the systems attempt to keep the free energy at a minimum, and in Monte Carlo simulations that have been performed the *swelling free energy* has been used to describe the stability of clays[41, 42, 43]. The swelling free energy can be expressed as a function of the separation z between the clay sheets [42]

$$\Delta E(z) = -L_x L_y \int_{z_0}^{z} [P_z(s) - P_{ext}] ds. \tag{3.1}$$

Here $L_x L_y$ is the area of the clay sheet, $P_z(s)$ is the pressure/stress component normal to the clay sheets when they are separated by a distance, s, apart and P_{ext} is the applied external pressure. z_0 is the reference spacing. Finding the minimum of this might look straight forward, since it basically only involves finding an expression for $P_z(s)$. However, $P_z(s)$ is determined by the temperature, the total number of interlayer guest molecules and the derivative of the potential energy [43]. The potential energy is again determined by Coulombic and van der Waals contributions and also stretch and bend terms when CO_2 is intercalated [12]. An expression for P_z which contains the transition between intercalation states will hence be very complex, since both the energy terms and the number of intercalated guest molecules will change during intercalation. In the Monte Carlo simulations mentioned above, the stability has been calculated only for system after intercalation, and even those calculations are too comprehensive to include here. A solution to equation 3.1 might be able to give a number for the eventual saturation value for the d-spacing (cf. the gentle curvature of the d-spacing in figure 3.15) after the main proportion of the clay

particles in the sample volume has intercalated CO_2, but not explain why the rate of the intercalation increase with increasing external pressure. The temperature dependence of $P_z(s)$ might be the reason why the rate of intercalation seems to depend on temperature (see figures 3.6 and 3.8).

Equation 3.1 yields a difference in d-spacing for different conditions of the external pressure. Unfortunately the measurement performed with an external pressure of 5 bar (see figure 3.17) had not intercalated enough CO_2 in comparison with the 15 bar experiment to verify this. And even if they would have, the difference given by the equation might even not be big enough to observe with WAXS. Bathija et al. [44] states that the basal spacing changes can be ignored for external pressure lower than 10 bar but that it shows maximum sensitivity to stress in the region 10 bar to 100 kbar. Since the two measurements (5 bar and 15 bar) represents each regions, this speaks in favor for that there might be a difference. However, further studies are needed to confirm this.

A intuitive reason for why the rate of the intercalation increase with the increase of pressure, is the fact that the reservoir of CO_2 molecules surrounding the clay particles increase with pressure. The number of particles is proportional to the pressure according to the ideal gas law, $PV = NkT$, when in the gaseous phase. With more particles available for intercalation, it is reasonable to think that this will lead to more intercalation. This relates to case of water vapor intercalation, where changing the relative humidity (i.e. by changing the temperature or pressure) regulates the surrounding reservoir, and by doing so determines if the reservoir acts as a source or a sink for the intercalated water.

In conclusion the model of free swelling energy might be able to explain some of the aspects of the intercalation process, especially the stabilization of the d-spacing with respect to temperature and pressure. It would however require a more detailed expression for the pressure normal to the clay sheets, if it is to model the dynamics of the intercalation process (cf. equation 3.1 does not include a time dependence). More experimental measurements for comparison between model and experimental results is of course also important and necessary.

Chapter 4

Concluding remarks

With no prior knowledge of how the NaFh interacts with CO_2, we have now been able to prove that it intercalates into the interlayer space of NaFh at conditions not too far from ambient. The mean basal d-spacing of the clay when CO_2 is intercalated has been calculated to be 12.38 ± 0.04 Å for the conditions -20°C and 15 bar. The expansion is indistinguishable from the change experienced in the 0WL-1WL hydration state transition, but the possibility of water intercalation has been ruled out through various measurements. The dynamics of the process has been observed to be dependent on the external pressure and temperature, with the decrease of temperature and the increase in pressure leading to a higher intercalation rate. The rate of intercalation could in any case be considered slow. The phase of CO_2 (i.e. gas or liquid) does not appear to have any major influence on the intercalation process. Existing molecular models based on the swelling free energy have been proposed as capable to describe some of the observed features.

Further studies

A suggestion for further WAXS studies is to perform more scans of NaFh exposed to CO_2 at different conditions for temperatur and pressure, hence mapping the dynamics of the intercalation process better. Also studies with pressurized air and NaFh at different temperature could be interesting and would allow to get a better understanding of the relationship between the external pressure, temperature and basal d-spacing of the clay. For futher studies with WAXS it also advisable to design a new sampleholder. Allthough fully functional, problems were accounted when cooling the sample holder down. This problem arised mainly because of the size and the big volume occupied by copper.

Since infrared spectroscopy has been used to show CO_2 intercalation in a 2:1 aluminosilicate [6], this technique might provide a better method for distinguishing the intercalated substances than WAXS.

Appendix A

1WL hydration states

In this appendix I present diffraction patterns (figureA.1) and a plot of the d-spacing (figureA.2) for measurements of the NaFh in the 1WL-hydration state carried out with the use of the NanoStar. Because of various reasons it was necessary to take measurements of the NaFh in the 1WL-state with the same experimental setup, for comparison with the samples exposed to CO_2. Eventual differences in d-spacing between intercalated water and CO_2 resulting from instrumental factors could then be ruled out. The first diffraction pattern cor-

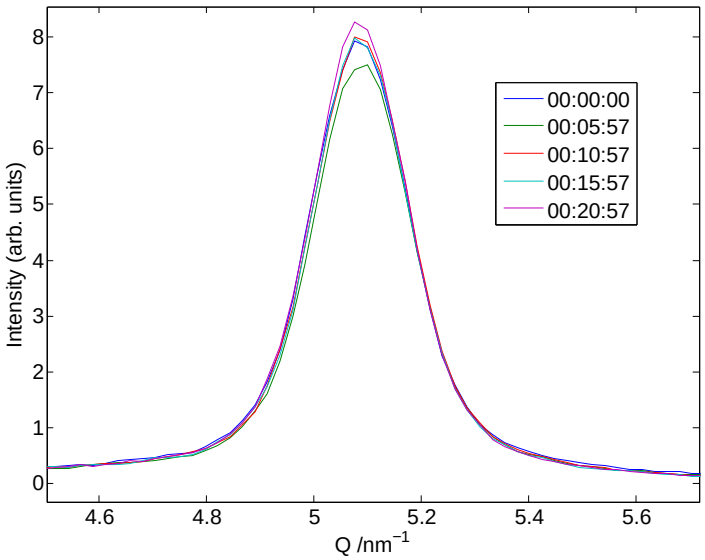

Figure A.1: Diffraction patterns from NaFh in the 1WL-state. The first pattern corresponds to measurement taken at ambient conditions, while the others corresponds to measurements taken at -20°C.

responds to a measurement taken at ambient conditions, while the others corresponds to measurements taken at -20°C.

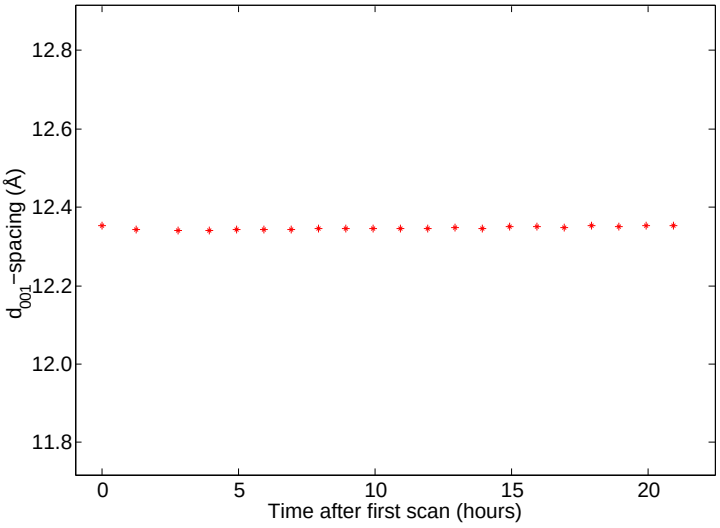

Figure A.2: Evolution of the d_{001}-spacing for the 1WL hydration state, when sample was held at -20°C and ambient pressure.

The mean basal spacing, based on the values in figure A.2, is $12.36 \pm 3.96 \times 10^{-4}$ Å. This value deviates some from the distance obtained at synchrotron measurements (12.24 ± 0.02 Å) [2]. However, those measurements were performed at a temperature of 30°C, which might explain the deviation.

Appendix B

CO_2 storage

Clay minerals have by some been mentioned as attractive materials for carbon capture [12]. With the results that I have presented, I thought it would be interesting to estimate the CO_2 storage capacity of NaFh through some simple calculations.

First I start with finding the mass of the unit cell and CO_2 molecule. This is simply done by summing the weight, times the amount, for each atom. For the NaFh I use the chemical formula $Na_{1.2}Mg_{4.8}Li_{1.2}Si_8O_{20}F_4$ [45] in calculation of the molecular weight. When I divide the weight with Avagadro's number, I obtain the mass in grams.

- Weight of the NaFh unit cell $= 1.2703 \times 10^{-21}\,\mathrm{g}$.
- Weight of the CO_2 molecule $= 7.305 \times 10^{-23}\,\mathrm{g}$.

G. J. da Silva et al. [2] estimated the proportion of water molecules to Na cations to be 2 for the 1WL case. Since CO_2 cause the same d-spacing shift, the ratio of intercalated CO_2 to cation can be considered more or less equal. Each unit cell of clay in the 0WL-state is then able to intercalate 2.4 CO_2 molecules. For each gram clay one can therefore store

$$1\,\mathrm{g} \cdot \frac{2.4 \cdot 7.305 \times 10^{-23}\,\mathrm{g}}{1.2703 \times 10^{-21}\,\mathrm{g}} \approx 0.14\,\mathrm{g} \tag{B.1}$$

of CO_2. Calculations performed by Statistics Norway [46] estimates the emission of CO_2 for energy consumption per capita in 2006 to be 7.9 tons. To store this amount you would then need over 56.4 tons of NaFh! The density of the clay in the intercalated state can be calculated quite easily if using the repetition distance we found in this experiment as the c-axis and the value given by Kalo et al. [45] for the product of the ab unit axis.

- $ab = 47.3\,\mathrm{Å}^2, c = 12.35\,\mathrm{Å}, V = 5.8416 \times 10^{-22}\,\mathrm{cm}^3$.

We then get a density of

$$p = \frac{1.2703 \times 10^{-21}\,\mathrm{g} + 2.4 \cdot 7.305 \times 10^{-23}\,\mathrm{g}}{5.8416 \times 10^{-22}\,\mathrm{cm}^3} = 2.47\,\mathrm{g/cm}. \tag{B.2}$$

56.4 tons of NaFh intercalated with CO_2 will occupy an area of approximately 26 cubic meters. If we calculate with a porosity of 50% [47], the total area will be closer to 50 cubic meters. In other words one can not expect each person to dig down and store his share of the nations CO_2 emmision from energy consumption in his own garden. However this could be a possible solution for industries which are located in areas that are rich on swelling clays.

Bibliography

[1] H. Hemmen, L. R. Alme, J. O. Fossum, and Y. Meheust, "X-ray studies of interlayer water absorption and mesoporous water transport in a weakly hydrated clay," *Phys. Rev. E*, vol. 82, p. 036315, 2010.

[2] G. J. da Silva, J. O. Fossum, E. DiMasi, K. J. Måløy, and S. B. Lutnæs, "Synchrotron X-ray scattering studies of water intercalation in a layered synthetic silicate," *Phys. Rev. E*, vol. 66, p. 011303, 2002.

[3] G. J. da Silva, J. O. Fossum, E. DiMasi, and K. J. Måløy, "Hydration transitions in a nanolayered synthetic silicate: A synchrotron X-ray scattering study," *Phys. Rev. B*, vol. 67, p. 094114, 2003.

[4] G. Løvoll, B. Sandnes, Y. Méheust, K. J. Måløy, J. O. Fossum, G. J. da Silva, M. S. P. Mundim, R. D. Jr., and D. M. Fonseca, "Dynamics of water intercalation fronts in a nano-layered synthetic silicate: A synchrotron X-ray scattering study," *Physica B*, vol. 370, pp. 90–98, 2005.

[5] J. Fripat, M. I. Cruz, B. F. Bohor, and J. Thomas, "Interlamellar adsorption of carbon dioxide by smectites," *Clays and Clay Minerals*, vol. 22, pp. 23–30, 1974.

[6] L. Wang, M. Zhang, and S. A. T. Redfern, "Infrared study of CO_2 incorporation into pyrophyllite $[Al_2Si_4O_{10}(OH)_2]$ during dehydroxylation," *Clays and Clay Minerals*, vol. 51, pp. 439–444, 2003.

[7] J. O. Fossum, "Physical phenomena in clays," *Physica A*, vol. 270, p. 270, 1999.

[8] F. Bergaya, B. Theng, and G. Lagaly, *Handbook of Clay Science*. Amsterdam: Elsevier, 2006.

[9] T. N. Blanton, D. Majumdar, and S. M. Melpolder, "Microstructure of clay-polymer composites," *International Centre for Diffraction Data 2000, Advances in X-ray Analysis*, vol. 42, pp. 562–568, 2000.

[10] S. A. Solin, "Clays and clay intercalation compounds: Properties and physical phenomena," *Annu. Rev. Mater. Sci.*, vol. 27, pp. 89–115, 1997.

[11] J. Bujdak, "Effect of the layer charge of clay minerals on optical properties of organic dyes. a review," *Applied Clay Science*, vol. 34, pp. 58–73, 2006.

[12] R. T. Cygan, V. N. Romanov, and E. M. Myshakin, "Natural materials for carbon capture," tech. rep., Sandia National Laboratories, Albuquerque, New Mexico, U.S.A., November 2010.

[13] P. D. Kaviratna, T. J. Pinnavaia, and P. A. Schroeder, "Dielectric properties of smectite clays," *J. Phys. Chem Solids*, vol. 57, pp. 1897–1906, 1996.

[14] P. Patnaik, *Handbook of Inorganic Chemicals*. McGraw-Hill, 2003.

[15] "Acting on climate change: The UN system delivering as one." `http://www.un.org/climatechange/pdfs/Acting\%20on\%20Climate\%20Change.pdf` (2011-25-04), November 2008.

[16] B. Metz, "IPCC special report on carbon dioxide capture and storage," tech. rep., Intergovernmental Panel on Climate Change, 2005.

[17] P. Pyykkö and M. Atsumi, "Molecular double-bond covalent radii for elements Li-E112," *Chem. Eur. J.*, vol. 15, p. 12770–12779, 2009.

[18] "All nobel prizes in physics." `http://nobelprize.org/nobel_prizes/physics/laureates/` (2011-25-04).

[19] W. Friedrich, P. Knipping, and M. Laue, "Interferenzerscheinungen bei röntgenstrahlen," *Annalen der Physik*, vol. 346, no. 10, p. 971–988, 1913.

[20] D. M. J. Als-Nielsen, *Elements of Modern X-ray Physics*. Chichester: Wiley, 2001.

[21] D. Moore and J. Reynholds, *X-Ray Diffraction and the Identification and Analysis of Clay Minerals*. New York: Oxford University Press, 2nd ed., 1997.

[22] G. Strobl, *Condensed Matter Physics*. Berlin: Springer, 2004.

[23] B. B. He, *Two-Dimensional X-Ray Diffraction*. New Jersey: Wiley, 2009.

[24] P. P. Ewald, "Das reziproke gitter in der strukturtheorie," *Z. Kristallogr.*, vol. 56, p. 129, 1921.

[25] J. R. C. Reynolds, "The lorentz-polarization factor and preferred orientation in oriented clay aggregates," *Clays and Clay Minerals*, vol. 34, pp. 359–367, 1986.

[26] P. Thompson, D. E. Cox, and J. B. Hastings, "Rietveld refinement of debye-scherrer synchrotron X-ray data from Al_20_3," *J. Appl. Cryst.*, vol. 20, pp. 79–83, 1987.

[27] R. N. Bracewell, *The Fourier Transform and Its Applications*. New York: McGraw-Hill, 1986.

[28] G. K. Wertheim, M. A. Butler, K. W. West, and D. N. E. Buchanan, "Determination of the gaussian and lorentzian content of experimental line shapes," *Rev. Sci. Instrum.*, vol. 45, pp. 1369–1371, 1974.

[29] S. Hendricks and E. Teller, "X-ray interference in partially ordered layer lattices," *J. Chem. Phys.*, vol. 10, pp. 147–167, 1942.

[30] A. G. Michette and C. J. Buckley, *X-RAY SCIENCE AND TECHNOLOGY*. Bristol: Institute of Physics Publishing, 1993.

[31] H. Wiedemann, *Synchrotron Radiation*. Berlin: Springer, 2003.

[32] H. Winick, *Synchrotron Radiation Sources; A Primer*. Berlin: World Scienific, 1994.

[33] C. Cocco and M. Zangrando, *Magnetism and Synchrotron Radiation; New Trends*, ch. Synchrotron Radiation Sources and Optical Devices. Berlin, Heidelberg: Springer, 2010,.

[34] Y. Cerenius, K. Ståhl, L. A. Svensson, T. Ursby, . Oskarsson, J. Albertsson, and A. Liljasa, "The crystallography beamline I711 at MAX II," *J. Synchrotron Rad.*, vol. 7, pp. 203–208, 2000.

[35] T. Huang, H. Toraya, T. Blanton, and Y. Wu, "X-ray powder diffraction analysis of silver behenate, a possible low-angle diffraction standard," *J. Appl. Cryst.*, vol. 26, pp. 180–184, 1993.

[36] D. M. Fonseca, Y. Méheust, J. O. Fossum, K. D. Knudsen, and K. P. S. Parmar, "Phase diagram of polydisperse Na-fluorohectorite–water suspensions: A synchrotron small-angle X-ray scattering study," *Phys. Rev. E*, vol. 79, p. 021402, 2009.

[37] H. Hemmen, "Clay powder swelling, source or sink?." Unpublished work, 2011.

[38] L. A. G. Aylmore, "Microporosity in montmorillonite from nitrogen and carbon dioxide sorption," *Clays and Clay Minerals*, vol. 25, pp. 148–154, 1977.

[39] R. H. Perry and D. W. Green, *Perry's chemical engineers handbook*. New York: McGraw-Hill, 2008.

[40] R. Tenorio, L. Alme, M. Engelsberg, J. O. Fossum, and F. Hallwass, "Geometry and dynamics of intercalated water in Na-Fluorohectorite clay hydrates," *J. Phys. Chem. C*, vol. 112, pp. 575–580, 2008.

[41] M. Chavez-Paez, L. dePablo, and J. J. dePablo, "Monte carlo simulations of Ca–montmorillonite hydrates," *J. Chem. Phys.*, vol. 114, no. 24, pp. 10948–10953, 2001.

[42] Y. Yu and X. Yang, "Molecular simulation of swelling and interlayer structure for organoclay in supercritical CO_2," *Phys. Chem. Chem. Phys.*, vol. 13, pp. 282–290, 1987.

[43] R. M. Shroll and D. E. Smith, "Molecular dynamics simulations in the grand canonical ensemble: Application to clay mineral swelling," *J. Chem. Phys.*, vol. 111, no. 19, pp. 9025–9033, 1999.

[44] A. P. Bathija, H. Liang, N. Lu, M. Prasad, and M. L. Batzle, "Stressed swelling clay," *GEOPHYSICS*, vol. 74, no. 4, pp. A47–A52, 2009.

[45] H. Kalo, M. W. Möller, M. Ziadeh, D. Dolejš, and J. Breu, "Large scale melt synthesis in an open crucible of na-fluorohectorite with superb charge homogeneity and particle size," *Applied Clay Science*, vol. 48, p. 39–45, 2010.

[46] "Utslipp til luft av karbondioksid fra energibruk." `http://www.ssb.no/aarbok/tab/tab-042.html` (2011-06-05).

[47] K. Knudsen, J. O. Fossum, G. Helgesena, and M. Haakestad, "Small-angle neutron scattering from a nano-layered synthetic silicate," *Physica B*, vol. 352, p. 247–258, 2004.